REPORT DOCUMENTATION PAGE

AFRL-SR-AR-TR-04-

0484

1. REPORT DATE *(DD-MM-YYYY)* 18-08-2004	**2. REPORT TYPE** Final	**3. DATES COVERED** *(From - To)* Feb 2001 - Aug 2004

4. TITLE AND SUBTITLE **CONTROL OF MIXING IN SHEAR FLOWS**	**5a. CONTRACT NUMBER** F49620-01-C-0021
	5b. GRANT NUMBER
	5c. PROGRAM ELEMENT NUMBER
6. AUTHOR(S) Banaszuk, Andrzej	**5d. PROJECT NUMBER**
	5e. TASK NUMBER
	5f. WORK UNIT NUMBER
7. PERFORMING ORGANIZATION NAME(S) AND ADDRESS(ES) United Technologies Research Center MS129-15 411 Silver Lane East Hartford, CT 06108	**8. PERFORMING ORGANIZATION REPORT NUMBER**
9. SPONSORING / MONITORING AGENCY NAME(S) AND ADDRESS(ES) Lt Col Sharon Heise, PhD Program Manager, Dyn.& Contr. AFOSR/NM, 4015 Wilson Blvd, Rm 713, Arlington, VA 22203	**10. SPONSOR/MONITOR'S ACRONYM(S)** AFOSR/NM
	11. SPONSOR/MONITOR'S REPORT NUMBER(S)

12. DISTRIBUTION / AVAILABILITY STATEMENT
Unclassified, Unlimited Distribution

DISTRIBUTION STATEMENT A
Approved for Public Release
Distribution Unlimited

13. SUPPLEMENTARY NOTES

14. ABSTRACT

The objective of this research was to develop tools for modeling, analysis, and control design for unsteady non-equilibrium flow phenomena relevant to operation of aeroengines, such as shear flows, thermoacoustic instabilities, and flutter. Methods for enhancing mixing in jets in cross flow using flow control were developed and demonstrated in experiments. Control of Pattern Factor using jet in cross flow control was demonstrated in a rig experiment. A hierarchy of models for control of thermoacoustic instabilities and flutter was developed and applied to analysis of dynamics and control design. The most important theoretical accomplishment of the current research was establishment of a framework for studying fundamental limitations of achievable performance in control of oscillations described by nonlinear models, including delays, and driven by broad-band noise.

15. SUBJECT TERMS

Control, Adaptive, Fundamental Limitations of Performance, Nonlinear Dynamics, Jet Engines, Flow Control, Mixing, Pattern Factor, Thermoacoustic Instability, Flutter

16. SECURITY CLASSIFICATION OF: **None**			**17. LIMITATION OF ABSTRACT**	**18. NUMBER OF PAGES**	**19a. NAME OF RESPONSIBLE PERSON** Andrzej Banaszuk
a. REPORT SAR	**b. ABSTRACT** SAR	**c. THIS PAGE** SAR	SAR	69	**19b. TELEPHONE NUMBER** *(include area code)* *860.610.7381*

Standard Form 298 (Rev. 8-98)
Prescribed by ANSI Std. Z39.18

20040922 014

CONTROL OF MIXING IN SHEAR FLOWS

CONTRACT F49620-01-C-0021

FINAL REPORT

Andrzej Banaszuk
United Technologies Research Center,
MS129-15,
411 Silver Lane,
East Hartford, CT 06108,
tel. 860 610 7381, `banasza@utrc.utc.com`

0.1 Objectives

The objective of this research was to develop approach to control of mixing in shear flows and apply it to control of pattern factor and thermoacoustic instabilities in military aeroengines. A more general objective was to develop tools for modeling, analysis, and control design for unsteady non-equilibrium flow phenomena relevant to operation of aeroengines.

0.2 Summary of Accomplishments

The original objective of developing methods for control of mixing relevant to pattern factor control was accomplished. Methods for enhancing mixing in jets in cross flow using flow control were developed and demonstrated in experiments. Control of Pattern Factor using jet in cross flow control was demonstrated in a rig experiment. This work is described in Section 2.1.

The objective of controlling thermoacoustic instabilities via mixing control was not accomplished. The funding was re-directed towards more promising fuel control of thermoacoustic instabilities. The decision was based on the fact that the fuel flow control was considered more feasible than air flow control and more likely to be transitioned to a 6.2 project on Active Screech Control (jointly funded by Air Force Research Lab and Pratt & Whitney).

In the area of fuel control several accomplishements are worth mentioning. First, a hierarchy of models for control of thermoacoustic instabilities was developed. A method of control of flame front was demonstrated in a distributed model. Control of rotating waves arising as results of thermoacoustic instability on a annular domain was demonstrated in a reduced order model. The effect of combustion on the fluid dynamics was analyzed in a distributed and reduced order models. The results are presented in Section 2.2. Other accomplishments include analysis of impact of symmetry-breaking (Section 2.3) and external noise (Section 2.4) on thermoacoustic instabilities. The study of the fundamental limitations of achievable performance described in the next paragraph was motivated by the control of thermoacoustics.

The most important theoretical accomplishment of the current research was establishment of a framework for studying fundamental limitations of achievable performance in control of oscillations described by *nonlinear* models, including delays, and driven by broad-band noise described in Section 1.1. The framework is based on frequency domain formulation of model response. While linear dynamic components (oscillators and delays) are easy to handle in the frequency domain, the challenge was the treatment of static nonlinearities. This was accomplished by replacing the nonlinearities by their *Random Input Describing Functions.* This approach was very effective in studying limitations of performance in fuel control of thermoacoustic instabilities using on-off fuel valves. The framework involved *approximations.* As a first step towards a fully rigorous framework for analysis of nonlinear ocillations, the *Spectral Balance* approach (Section 1.2) was introduced and demonstrated in an example of a nonlinear model with multiple attractors. Other accomplishments include introduction of two methods of adaptive control of oscillations with uncertain parameters (Section 1.3) and analysis of uncertainty propagation in complex, interconnected dynamical systems (Section 1.4).

Finally, a linear framework for control of wave phenomena on annular domain was established. The flutter control problem described in Section 2.5 was used to motivate the study.

The results of the current research are summarized in 11 journal papers (5 published, 3 in print, 3 submitted) and 20 conference papers. Three invited sessions were organized with support from current grant.

0.3 Organization of the report

We provide extended abstract for the results that are published and hence easily available. We provide more details for the results that are not available, like papers that are submitted or in the case of ungoing research. List of references is available in the last two chapters of the report. References to journal papers that were written under this contract are referenced with letter "j" in front ([j1], [j2], etc.). Conference papers written under this contract are referenced with letter "c" in front ([c1], [c2], etc.).

Contents

Chapter 1

Control Theory for Nonlinear Oscillations in Military Aeroengines

1.1 Analysis of fundmental limitations of achievable performance in control of oscillations in nonlinear systems

The most important theoretical accomplishment of the current research was establishment of a framework for studying fundamental limitations of achievable performance in control of oscillations described by *nonlinear* models, including delays, and driven by broad-band noise. The framework is based on frequency domain formulation of model response. While linear dynamic components (oscillators and delays) are easy to handle in the frequency domain, the challenge is the treatment of static nonlinearities. This was accomplished by replacing the nonlinearities by their *Random Input Describing Functions.* This approach was very effective in describing limitations of performance in fuel control of thermoacoustic instabilities using on-off fuel valves. The framework involved *approximations.* As a first step towards a fully rigorous framework for analysis of nonlinear ocillations, the *Spectral Balance* approach was introduced and demonstrated on an example of a nonlinear model with multiple attractors.

1.1.1 Fundamental limitations of achievable performance in control of thermoacoustic instabilities

Thermoacoustic instabilities in gas turbine and rocket engines develop when acoustic waves in combustors couple with an unsteady heat release field in a positive feedback loop. Fuel control was demonstrated to be an effective way of reducing the level of pressure oscillation in combustors [46] [6] [7] [30] [23] [17] [11] [24] [45]. However, the achieved reduction of pressure oscillation between experiments ranges from 6dB to 20dB [11] [24]. Moreover, in some cases the attenutation of the oscillation at primary frequency is accompanied by excitation of the oscillation in some other frequency band [6] [7] [30] [17] [45]. This phenomenon is refered to as *secondary peaks* or *peak splitting.*

Until recently, the question of what are the factors that impact the achievable level of attenuation of pressure oscillations with active fuel control was not addressed. In particular, the cause of the peak splitting phenomenon (two peaks in the pressure spectrum with control) observed in many combustion experiments [6] [7] [30] [17] [45] did not have a satisfactory explanation. One of the reasons was that the majority in the thermoacoustic instability control community believed that the thermoacoustic instability arises only as a stability loss leading to a limit cycling behavior (one peak in the pressure spectrum), and any control action stabilizing the equilibrium of the thermoacoustic system will result in quenching the oscillations (no peaks).

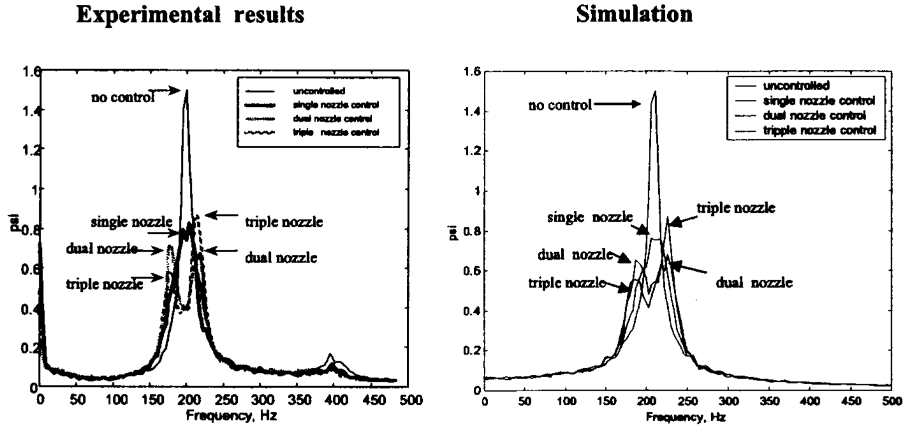

Figure 1.1: PSD of pressure signal with on/off control of one, two, or three liquid fuel nozzles. The peak splitting phenomenon observed in experiment reproduced in reduced order model simulation.

Two major contributions of the UTRC combustion control team (including academic partners) were:

1. A method for determining whether a given combustor should be modeled as a limit cycling or a noise-driven stable system [37, 38].
2. Analysis of factors that affect the achievable level of suppression of pressure oscillations for both stable and limit-cycling systems [13, 12, 3, 4, 2].

The analysis of the data from combustion experiments has shown that industrial combustors are often described by stable, linear, noise-driven models. Standard frequency domain methods were applied to such models showing that in some conditions the transport delays and limited actuator bandwidth fundamentally limit the level of achievable suppression of the pressure oscillations [3]. The origin of the peak-splitting was explained using stable linear models with large delay in actuation due to the fuel transport process.

Under the current contract, the frequency domain fundamental limitation were extended to nonlinear combustion models, including the limit cycling ones [4, 2].

The peak-splitting phenomenon was observed in DARPA-sponsored sector rig experiments and was reconstructed in a model (see Figure 1.1). Because on/off valves were used for control, a linear analysis was not applicable. However, a nonlinear analysis involving Random Input Describing Functions [13, 12, 2, 24, 3, 4] allowed an explanation of the phenomenon. It has been shown that, as in the linear model case, the pressure oscillations cannot be arbitrarily suppressed due to non-minimum phase effects (transport delay) and limited actuator bandwidth. It was also shown that the effects of the driving disturbances and saturation nonlinearities needs to be incorporated in the analysis. The sector rig model was derived in the form of a feedback interconnection of a stable linear transfer function $G_0(j\omega)$, and a relay nonlinearity $f(\cdot)$, subject to a driving disturbance $N(j\omega)$ as

$$X(j\omega) = G_0(j\omega)(N(j\omega) - Y(j\omega)) \tag{1.1}$$

$$y(t) = f(x(t)). \tag{1.2}$$

for $G_0(j\omega) = G_1(j\omega)G_c(j\omega)$. $G_1(j\omega)$ represented the serial connection of the thermoacoustic response to fuel valve output dominated by a single resonant mode with a natural frequency of about 200Hz and a non-minimum phase transfer function representing the transport delay from the fuel injection location to the flame. $G_c(j\omega)$ was the transfer function of a phase-shifting controller used in the experiment. The nonlinearity was representing the relay characteristic on the on-off valves.

In the Random Input Describing Function [20] analysis one assumes that the input $u(t)$ to the nonlinear element is of the form $u(t) = B + A\sin(\omega t + \theta) + r(t)$, where B, A, ω are unknown constants, θ is an arbitrary initial phase, and $r(t)$ is a Gaussian process with a standard deviation σ. The output of the nonlinear element $y(t) = f(u(t))$ is approximated as

$$y_a(t) = N_B B + N_A A\sin(\omega t + \theta) + N_R r(t), \tag{1.3}$$

where the individual gains (called Describing Functions of the nonlinearity) are obtained by minimization of the variance of the residual:

$$\begin{aligned} N_B(B,A,\sigma) &= \tfrac{1}{B}E[f(u(0))] = \\ &\frac{1}{(2\pi)^{\frac{3}{2}}\sigma B}\int_0^{2\pi} d\theta \int_{-\infty}^{\infty} dr f(B + A\sin(\theta) + r)\exp(-\tfrac{r^2}{2\sigma^2}), \end{aligned} \tag{1.4}$$

$$\begin{aligned} N_R(B,A,\sigma) &= \tfrac{1}{\sigma^2}E[f(u(0))r(0)] = \\ &\frac{1}{(2\pi)^{\frac{3}{2}}\sigma^3}\int_0^{2\pi} d\theta \int_{-\infty}^{\infty} dr f(B + A\sin(\theta) + r) r \exp(-\tfrac{r^2}{2\sigma^2}), \end{aligned} \tag{1.5}$$

$$\begin{aligned} N_A(B,A,\sigma) &= \tfrac{2}{A}E[f(u(0))\sin(\theta)] = \\ &\frac{2}{(2\pi)^{\frac{3}{2}}\sigma A}\int_0^{2\pi} d\theta \int_{-\infty}^{\infty} dr f(B + A\sin(\theta) + r)\sin(\theta)\exp(-\tfrac{r^2}{2\sigma^2}). \end{aligned} \tag{1.6}$$

([20], p. 371). For the no-noise and no-bias case where $r(t) = 0$ and $B = 0$, the last formula reduces to the standard sinusoidal input describing function gain.

This framework easily allows us to study the response of the pressure output in either open or closed loop thermoacoustic system as an output of a stable noise driven system (when $A = 0$) or as self-excited oscillation (when $A > 0$) or some combination of the two. We assume the Gaussian component $r_i(t)$ of the input disturbance has Power Spectral Density $\Phi_{ii}(j\omega)$ and write corresponding equations:

1. Stable driven system

$$B = \frac{G_0(0)}{1 + N_B(B,A,\sigma)G_0(0)}B_i \tag{1.7}$$

$$A = \frac{G_0(j\omega)}{1 + N_A(B,A,\sigma)G_0(j\omega)}A_i \tag{1.8}$$

$$\Phi_{xx}(j\omega) = \left|\frac{G_0(j\omega)}{1 + N_R(B,A,\sigma)G_0(j\omega)}\right|^2\Phi_{ii}(j\omega) \tag{1.9}$$

$$\sigma^2 = \frac{1}{2\pi}\int_{-\infty}^{\infty}\Phi_{xx}(j\omega)d\omega. \tag{1.10}$$

2. Self-excited oscillations with driving noise

$$B = \frac{G_0(0)}{1 + N_B(B,A,\sigma)G_0(0)}B_i \tag{1.11}$$

$$1 + N_A(B,A,\sigma)G_0(j\omega) = 0 \tag{1.12}$$

$$\Phi_{xx}(j\omega) = \left|\frac{G_0(j\omega)}{1 + N_R(B,A,\sigma)G_0(j\omega)}\right|^2\Phi_{ii}(j\omega) \tag{1.13}$$

$$\sigma^2 = \frac{1}{2\pi}\int_{-\infty}^{\infty}\Phi_{xx}(j\omega)d\omega, \tag{1.14}$$

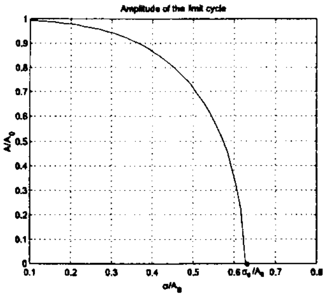

Figure 1.2: The amplitude of the limit cycle in the presence of the Gaussian noise

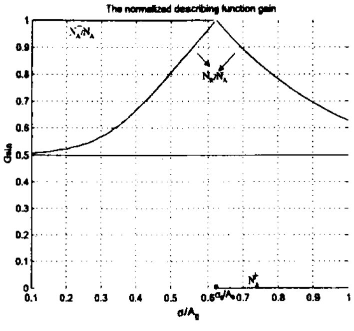

Figure 1.3: Describing function gains in the presence of Gaussian noise

For relay nonlinearity, the amplitude of the limit cycle can be found from solving the loop equation (1.12)

$$1 + N_A(A, \sigma)G_0(j\omega) = 0. \tag{1.15}$$

In Mehta *et al.*, IFAC 2002, we prove that for a relay nonlinearity:

1. For $\sigma \to 0$, the appearance of the limit cycle stabilizes the loop with respect to the noise thereby yielding a bounded input-output response (for the Gaussian noise driver) as solution of equation (1.13) and

2. for $\sigma \to \infty$, large noise stabilizes the loop with respect to the limit cycle thereby causing the limit cycle to disappear and the system to behave as a stable noise driven system.

More precisely, Figure 1.2 shows that the presence of noise ($\sigma > 0$) leads to a reduction in the amplitude of this limit cycle and at a critical positive value of $\sigma = \sigma_0$, the limit cycle disappears ($A(\sigma_0) = 0$ for values of $\sigma > \sigma_0$). Figure 1.3 shows the gains $N_R(\sigma)$ and $N_A(\sigma)$ as function of σ. For the values of σ where limit cycle is present, N_R monotonically increases between 0 and σ_0 and decreases for values of $\sigma > \sigma_0$. We also showed that the feedback interconnection of $G_0(j\omega)$ and $N_R(A(\sigma), \sigma)$ is linearly stable for all $\sigma \neq \sigma_0$ and the largest loop gain occurs at the critical value σ_0 where the loop is arbitrarily close to destabilization (eigenvalues on the imaginary axis). For values of σ away from σ_0, the eigenvalues move in to the LHP thereby ensuring asymptotic stability for all $\sigma \neq \sigma_0$.

Therefore, except for a critical $\sigma = \sigma_0$, the Fourier transform of the Gaussian component of combustor pressure may be approximated as

$$p_g(j\omega) = G_0(j\omega)S(j\omega, A, \sigma)n_i(j\omega), \tag{1.16}$$

where $r_i(j\omega)$ is the Fourier transform of the driving disturbance and

$$S(j\omega, A, \sigma) = \frac{1}{1 + G_0(j\omega)N_R(0, A, \sigma)G_c(j\omega)} \tag{1.17}$$

is a ***modified sensitivity function*** that depends on the magnitude of the limit cycle A and standard deviation σ of the Gaussian component at the input of the relay nonlinear element. This result allows to extend the results of the standard linear fundamental limitations analysis presented in the papers [2, 3, 4] to the case of control with on-off actuators. In particular, it can be shown that the supression of the pressure oscillations in the central frequency band of the natural combustor resonance (which requires $|S(j\omega, A, \sigma)| < 1$) will lead to amplification of the pressure oscillations in an adjacent frequency band ($|S(j\omega, A, \sigma)| > 1$), which leads to peak-splitting. The norm used here is the H_∞ norm.

Analysis presented here indicates that the peaking phenomenon defined as excitation of oscillations with closed-loop control is to a large extent inevitable for combustion processes with large delay controlled with actuators of limited bandwidth.

In Teerlinck *et al.*, 2005, we applied the nonlinear frequency-domain framework described above to explain results in active fuel control experiment in 800kW three-flameholder rig. The experiment involved on-off valves and severe peak-splitting was observed. The optimal amount of fuel was proposed to reduce the peaking and to provide acceptable attenutation of oscillations.

1.2 Spectral Balance

A frequency-domain framework for analysis, computations, and uncertainty propagation in nonlinear systems driven by broad-band disturbances was introduced and illustrated in a simple example of a nonlinear system that exhibits noise-induced transitions between two locally stable equilibria. An approximate and iterative spectral balance (including determination of equilibria) is solved. The solution of the approximate spectral balance is used to reformulate the original model using a loop transformation so that an iterative procedure for finding the spectrum of the output converges to the true spectrum of the solution. The work is presented in paper by Banaszuk and Mehta, CDC 2004.

Many industrial flows involve complex interactions of acoustic waves, vorticity, fuel transport, and chemical reactions. The control objective often is to create beneficial non-equilibrium dynamics with control. Examples include control of flow separation and mixing enhancement. In this paper we introduce a frequency domain framework for analysis and non-equilibrium control design for a large class of models of physical phenomena involving multiple oscillatory modes coupled through nonlinear terms, transport delay, and driven by broad-band disturbances. While motivated by specific problems arising in military aeroengines, the methods will be applicable to large class of distributed dynamical systems involving oscillatory dynamics with nonlinear cross-coupling, saturated nonlinearities, transport delay, and broad-band disturbances.

The *spectral balance* framework that we propose generalizes the standard harmonic balance and Gaussian signal balance in feedback systems [31, 20]. The framework is introduced and illustrated in an example of a nonlinear system that exhibits noise-induced transitions between two stable equilibria. The example presented is a scalar model with cubic nonlinearity after pitchfork bifurcation driven by a broad-band disturbance. An approximate and iterative spectral balance of the constant and broad-band signals (including determination of equilibria) is solved. The solution of this approximate spectral balance is used to reformulate the original model using a loop transformation so that an iterative procedure for finding the spectrum of the output converges to the true spectrum.

Consider a model of a lightly damped stable linear system with transfer function $G_0(j\omega)$, in a feedback loop with a static nonlinearity $f(\cdot)$, subject to a driving disturbance $n(t)$ with the Fourier transform $N(j\omega)$. An uncertainty in the model is represented by an (in general nonlinear) operator $\Delta(\cdot)$ in a feedback loop around the nominal model The model equations are

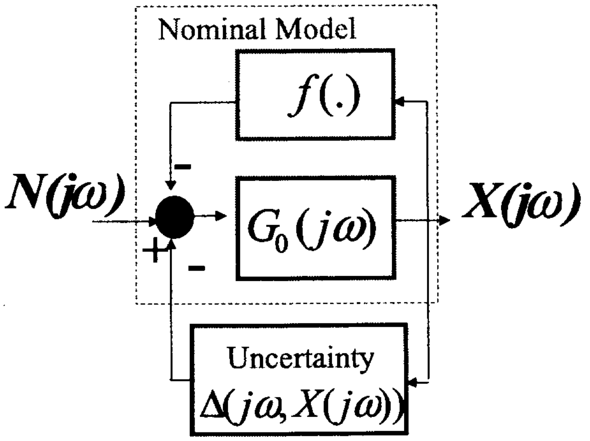

Figure 1.4: The model structure

$$X(j\omega) = G_0(j\omega)(N(j\omega) - \Delta(j\omega, X(j\omega)) - Y(j\omega)) \tag{1.18}$$

$$y(t) = f(x(t)) \tag{1.19}$$

where, $X(\cdot) = \mathcal{F}x(\cdot)$, $Y(\cdot) = \mathcal{F}y(\cdot)$, and $N(\cdot) = \mathcal{F}n(\cdot)$, are the Fourier transforms of the corresponding temporal signals. We assume that nonlinear mapping $f(\cdot)$ is Lipshitz on each bounded set. The equation (1.19) can be represented in the frequency domain as

$$Y(j\omega) = \hat{f}(X(j\omega)) := \mathcal{F}f(\mathcal{F}^{-1}X(j\omega)). \tag{1.20}$$

Now, the feedback system (1.18)–(1.19) can be represented as

$$X(j\omega) = G_0(j\omega)(N(j\omega) - \hat{f}(X(j\omega) - \Delta(j\omega)X(j\omega)). \tag{1.21}$$

Note that for the linear case $f(x) = 0$, $\Delta(j\omega, X(j\omega)) = \Delta(j\omega)X(j\omega)$ the mapping of the uncertainty $\Delta(j\omega)$ to the output of the system is given by the formula

$$X(j\omega) = (I + G_0(j\omega)\Delta(j\omega))^{-1}G_0(j\omega)N(j\omega). \tag{1.22}$$

involving the sensitivity function $(I + G_0(j\omega)\Delta(j\omega))^{-1}$. Note that the frequency domain representation greatly simplifies the uncertainty propagation analysis.

1. Uncertainty propagation. The sensitivity function $(I + G_0(j\omega)\Delta(j\omega))^{-1}$ allows to explicitly map the probability distribution of the uncertain parameters contributing to $\Delta(j\omega)$ to the probability distribution of the output $Y(j\omega)$.

2. The frequency domain representation greatly accelerates computation of this mapping. Note that only the algebraic calculations need to be performed in evaluating the formula (1.22). In contrast, a time domain counterpart of the (1.22) would require evaluation of the convolution integrals over long period of time. Computation of large linear systems with significantly separated time scales is cumbersome in time domain, as the shortest time scales detemine the time step size, while the longest time scales determine the total time of simulation. Moreover, in the time domain formulation one needs to wait for transients to subside, which is an issue when dealing with lightly damped dynamics. There are additional benefits of the frequency domain representation in the case when $G_0(j\omega)$ contains time delays.

3. Tools from the robust linear control theory allow to handle dynamic uncertainty in case when only the bounds on the uncertain operator are known [15].

Appart from application to the uncertainty propagation, the frequency domain formulation allows to study fundamental limitations of achievable control performance using methods of the complex analysis.

The *spectral balance* approach retains the advantages of the linear sensitivity function framework: explicit formulas mapping uncertainty to the output and the speed of computation. We will begin with the particular case of system in Figure 1.4 using the fixed point formulation (1.21). To introduce the spectral balance framework we will consider the case without uncertainty shown in Figure 1.5 with the corresponding fixed point formulation of the spectral balance equation given by (1.23)

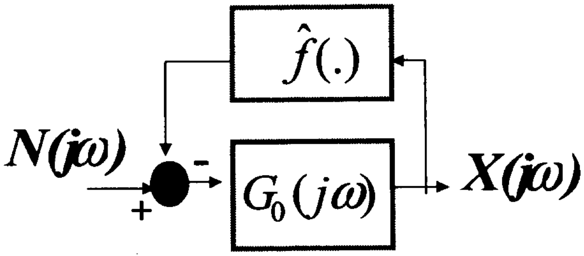

Figure 1.5: The model structure

$$X(j\omega) = G_0(j\omega)(N(j\omega) - \hat{f}(X(j\omega))). \tag{1.23}$$

Note that the spectral balance framework generalizes the standard harmonic balance (where the input signal $n(\cdot)$ is periodic, or when the dynamics has limit cycles) and Gaussian signal balance (where the input signal $n(\cdot)$ is a Gaussian broad band signal) in feedback systems [31, 20].

We assume that the dynamics of (1.19) is globally bounded and that there is an attractor. Eventually we intend to introduce a spectral balance framework for the class of *bounded power* signals on an infinite time interval. In this paper we restrict the attention to the space of L_2 signals on the interval $[0, T]$, where T is *large* relative to the slowest time scale in the system. The induced operator norms are the H_∞ norms.

A sufficient condition for existence of a *unique* solution of the spectral balance equation (1.23) is

$$||G_0(j\omega)(\hat{f}(X_2(j\omega)) - \hat{f}(X_1(j\omega)))|| < ||X_2(j\omega) - X_1(j\omega)||. \tag{1.24}$$

For all $X_i(j\omega)$ in $L_2[0,T]$. Note that in this case a unique solution to (1.23) exists (by applying the Banach Contraction Mapping Theorem [28]). Moreover, the approximate solution of the spectral balance equation can be obtained by successive approximations using the formula

$$X_{i+1}(j\omega) = G_0(j\omega)(N(j\omega) - \hat{f}(X_i(j\omega)). \tag{1.25}$$

with an arbitrary initial condition.

Note that if the condition (1.24) is satisfied for all $X_i(j\omega)$ in a closed set B in $L_2[0,T]$ that is invariant for the mapping $G_0(j\omega)(N(j\omega) - \hat{f}(\cdot))$, one can approach a solution of the spectral balance equation (1.23) in B using (1.25) with $X_0(j\omega) \in B$.

1.2.1 Loop transformation

A sufficient condition for (1.24) is the small gain condition for the feedback loop in (1.5). However, even if the condition (1.24) is not satisfied, which would be the case if the loop gain is large, one can attempt to enforce the condition (1.24) for an *equivalent* feedback system to (1.5) by a *loop transformation.* An example of a *linear* loop transformation is shown in Figure 1.6. Here $H(j\omega)$ is an arbitrary stable linear operator,

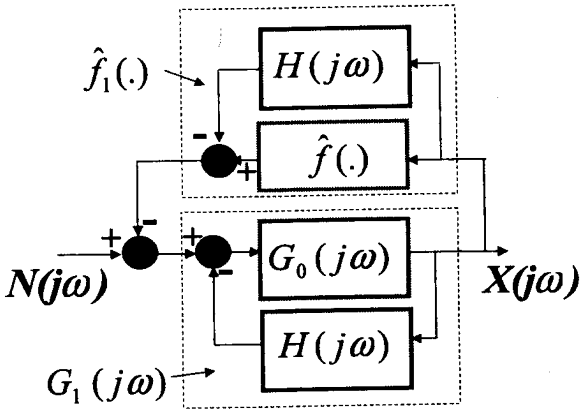

Figure 1.6: The loop transformation to enforce loop contractivity

$$G_1(j\omega) := (I + H(j\omega)G_0(j\omega))^{-1}G_0(j\omega). \tag{1.26}$$

and

$$\hat{f}_1(X(j\omega)) := \hat{f}(X(j\omega)) - H(j\omega)X(j\omega). \tag{1.27}$$

The spectral balance condition for the system in Figure 1.6 is

$$X(j\omega) = G_1(j\omega)(N(j\omega) - \hat{f}_1(X(j\omega)). \tag{1.28}$$

Note that a sufficient condition for the contraction condition for the *transformed* spectral balance (1.28) is

$$||G_1(j\omega)(\hat{f}_1(X_2(j\omega)) - \hat{f}_1(X_1(j\omega)))|| < ||X_2(j\omega) - X_1(j\omega)||. \tag{1.29}$$

If the nonlinear part of the loop in Figure 1.5 has a stabilizing effect, the role of the operator $H(j\omega)$ is to reduce the H_∞ gain of the nonlinear part of the loop and increase the contractivity of the linear part of the loop. More precisely, the gain of the nonlinear operator $\hat{f}(X(j\omega))$ is reduced by subtraction of a *linear* approximation of $\hat{f}(X(j\omega))$ and the approximate linear operator is incorporated in the linear part of the modified loop. Thus, a good choice of $H(j\omega)$ is the one that minimizes $||\hat{f}_1(X(j\omega))||$ for $X(j\omega)$ representing the solution of the spectral balance equation (1.28).

Of course, the minimization of $||\hat{f}_1(X(j\omega))||$ requires knowledge of $X(j\omega)$ itself, which is exactly the solution of the spectral balance equation that we seek. Note that we are interested in the case of system (1.19) having non-equilibrium attractors or subject to a large driving disturbance, so that an approximation of nonlinear operator $\hat{f}(X(j\omega))$ by its linearization at $(X(j\omega) = 0$ is not suitable.

The key idea introduced in this paper is to proceed in the following three steps:

1. Find an *approximate* solution $X_{appr}(j\omega)$ close to $X(j\omega)$. For this, the describing function techniques, both for harmonic and random Gaussian signals, can be utilized. In fact, as we will show in the next section, it may be not necessary to find an approximate solution $X_{appr}(j\omega)$, but only few parameters describing such a solution, like its time average and the average power.

2. Utilize the knowledge of $X_{appr}(j\omega)$ (or the parameters describing it) to find a linear transformation $H(j\omega)$ that minimizes (or at least reduces) $||\hat{f}_1(X_{appr}(j\omega))|| = ||\hat{f}(X_{appr}(j\omega)) - H(j\omega)X_{appr}(j\omega)||$.

3. Use $H(j\omega)$ to define the loop transformation (1.26)–(1.27). If the contraction condition (1.29) is satisfied on a closed set B in $L_2[0,T]$ that is invariant for the mapping $G_1(j\omega)(N(j\omega) - \hat{f}_1(\cdot))$, one can approach a solution of the spectral balance equation (1.23) in B using the iterative process defined by
$$X_{i+1}(j\omega) = G_1(j\omega)(N(j\omega) - \hat{f}_1(X_i(j\omega)) \tag{1.30}$$

starting with an arbitrary $X_0(j\omega) \in B$.

At present it is not clear under what general conditions the procedure described above will result in finding solutions to the spectral balance equations. In the next section we will show one example of a system with nontrivial dynamics, for which that the procedure yields the desired result.

1.2.2 Example

Consider the equation
$$\dot{x}(t) + ax(t) + bx^3(t) = n(t). \tag{1.31}$$

Here we assume that $a < 0$, $b > 0$, and the input signal $n(\cdot)$ has zero mean and flat spectrum $|N(j\omega)| = \sigma_i$ for all ω. In the sequel we will refer to the input signal $n(\cdot)$ as *noise*, even though we emphasize that in this paper we only consider the deterministic case. Note that for $a = 0$ the system (1.31) undergoes a ***pitchfork bifurcation*** and the equilibrium $x = 0$ becomes unstable for all $a > 0$. Two locally stable equilibria occur at $x = \sqrt{-\frac{a}{b}}$ and $x = -\sqrt{-\frac{a}{b}}$. Note that for a small value of σ_i^2 the solution $x(t)$ will be close to one of the stable equilibria. For some higher value of σ_i^2 the solution $x(t)$ will be transitioning from a neighborhood of the one of the stable equilibria to the other, as shown in Figure 1.7. Note that the spectral balance equation for (1.31) is

$$X(j\omega) = \frac{1}{j\omega + a}(N(j\omega) - \hat{f}(X(j\omega)), \tag{1.32}$$

where $f(x) := bx^3$. Note that, since $a < 0$, the linear operator $\frac{1}{j\omega+a}$ is unstable, and the contraction condition (1.24) is not satisfied. However, the nonlinear operator $f(x)$ has a stabilizing effect, so that we can attempt to transform the loop to an equivalent one, for which the contraction condition is satisfied, as described in Section 1.2.1.

Let $\bar{x} := \frac{1}{T}\int_0^T x(t)dt$ denote the time average of $x(t)$ and let $x'(t) := x(t) - \bar{x}$ denote the deviation of $x(t)$ from its average value. Let $\sigma_x^2 := \frac{1}{T}\int_0^T x'(t)^2 dt$ denote the mean power of $x'(t)$. In what follows

Typical solution

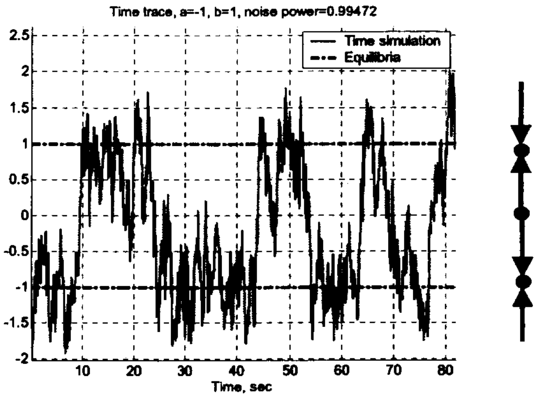

Figure 1.7: Typical solution of system (1.31): noise-induced transitions between two stable equilibria

we will compute *approximate* value of $\bar{x}$ and σ_x^2 by solving *approximate spectral balance* equations. By taking the time average of (1.33) and using the fact that the average of $(\bar{x}+x'(t))^3$ is $\bar{x}^3+3b\sigma_x^2$ we obtain

$$\bar{x}(a+3b\sigma_x^2+b\bar{x}^2)=\bar{n}=0. \tag{1.33}$$

Subtracting (1.33) from (1.31) and re-arranging terms yields

$$\dot{x}'(t)+(a+h)x'(t)+f_1(x'(t))=n(t), \tag{1.34}$$

where

$$h:=b\sigma_x^2+3b\bar{x}^2 \tag{1.35}$$

$$f_1(x'(t)):=b(x'^2-\sigma_x^2)(x'+3\bar{x}). \tag{1.36}$$

To find approximate values of $\bar{x}$ and σ_x^2 we will neglect the term $h(\bar{x},\sigma_x,x'(t))$ in (1.34) and solve the equation

$$\dot{x}'(t)+(a+b\sigma_x^2+3b\bar{x}^2)x'(t)=n(t). \tag{1.37}$$

Note that for fixed values of $\bar{x}$ and σ_x^2 (1.37) is a linear equation that can be solved in the frequency domain as

$$X'(j\omega)=\frac{N(j\omega)}{j\omega+a+b\sigma_x^2+3b\bar{x}^2}. \tag{1.38}$$

For a moment we assume that the values of $\bar{x}$ and σ_x^2 are such that $a+b\sigma_x^2+3b\bar{x}^2>0$, so that the transfer function $\frac{1}{j\omega+a+b\sigma_x^2+3b\bar{x}^2}$ us stable. This assumption will be verified after $\bar{x}$ and σ_x^2 are calculated.

Now we obtain the closure equation for σ_x^2 by integrating the absolute values of both sides of (1.38) over all frequencies

$$\sigma_x^2=\frac{1}{2\pi}\int_{-\infty}^{\infty}|\frac{\sigma_i}{j\omega+a+b\sigma_x^2+3b\bar{x}^2}|^2d\omega. \tag{1.39}$$

The equations (1.33) and (1.39) form an *approximate spectral balance* for the system (1.31. The integral in (1.39) can be analytically evaluated so that we can write the following equation

$$\sigma_x^2 = \frac{\sigma_i^2}{2(a + b\sigma_x^2 + 3b\bar{x}^2)}. \tag{1.40}$$

Now, solving (1.33) and (1.40) we obtain

$$\sigma_i^2 < \frac{a^2}{4b} \Rightarrow \tag{1.41}$$

$$\sigma_x^2 = \tfrac{|a|}{8b}(1 - \sqrt{1 - \tfrac{4b\sigma_i^2}{a^2}}), \tag{1.42}$$

$$\bar{x}^2 = -\tfrac{a}{b} - 3\sigma_x^2 \tag{1.43}$$

$$\sigma_i^2 > \frac{a^2}{4b} \Rightarrow \tag{1.44}$$

$$\sigma_x^2 = \tfrac{|a|}{2b}(1 + \sqrt{1 + \tfrac{2b\sigma_i^2}{a^2}}), \tag{1.45}$$

$$\bar{x} = 0. \tag{1.46}$$

Figure 1.8 graphically represents the solution to the approximate spectral balance equations as function of the input power σ_i for $a = -1$, $b = 1$. The solutions for $\bar{x}$ and σ_x^2 have a natural intepretation.

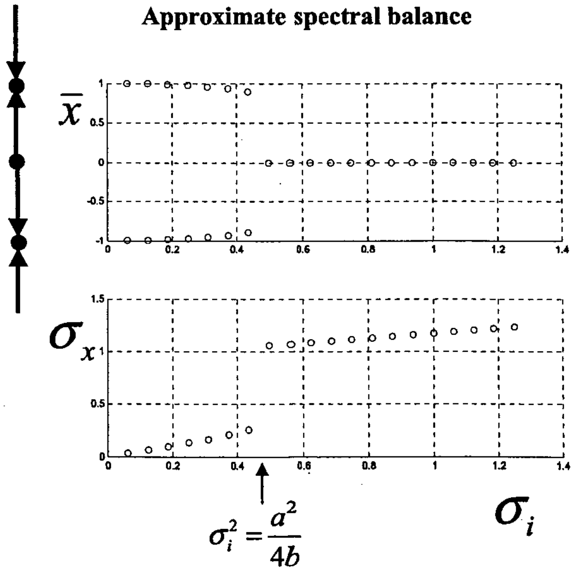

Figure 1.8: Solutions to approximate spectral balance equations as function of the input power

For $\sigma_i < \frac{a^2}{4b}$ there are two values of the time average $\bar{x}$ close to the no-noise equilibria that can be attained. The value of σ_x (that could be interpreted as standard deviation of $x(t)$) is small, so that the solution $x(t)$ stays close to an equilibrium solution and does not transition to the neighborhood of the other equilibrium. Above the critical value of the input power $\sigma_i = \frac{a^2}{4b}$ the solutions $x(t)$ deviate from the stable equilibria far enough to transition between the neighborhoods of the both equilibria. Since the transitions back and forth can occur, $\bar{x} = 0$ becomes the mean and the standard deviation σ_x is close to the distance from the new mean $\bar{x} = 0$ to the value where the solution $x(t)$ spends most of the time: close to the no-noise equilibria of (1.31).

We will now use the values of $\bar{x}$ and σ_x^2 given by (1.8) to perform a loop transformation as described in Section 1.2.1. More precisely, we will solve the perturbation equation (1.34) in the frequency domain using the fixed point formulation

$$X'(j\omega) = \frac{1}{j\omega + a + h}(N(j\omega) - \hat{f}_1(X'(j\omega)). \tag{1.47}$$

It can be easily verified that $a + h > 0$ for $\bar{x}$ and σ_x^2 given by (1.46). Analytic verification of the contraction condition for the operator $\frac{1}{j\omega+a+h}(N(j\omega) - \hat{f}_1(\cdot)$ is difficult. Therefore we will assume that the contraction condition is satisfied and proceed with an iterative solution to (1.47) using

$$X'_{i+1}(j\omega) = \frac{1}{j\omega + a + h}(N(j\omega) - \hat{f}_1(X'_i(j\omega)) \tag{1.48}$$

with $X'_0(j\omega) = 0$ and verify the contraction condition numerically. To illustrate and verify this procedure, a numerical solution of (1.31) for $a = -1$, $b = 1$, and $\sigma_i > \frac{a^2}{4b}$ was obtained. The spectrum $N(j\omega)$ of the noise from the time domain simulation was saved and used in the formula (1.48). Figure 1.9 shows an excellent agreement of the spectrum $X'(j\omega)$ from the time domain simulation and the spectrum $X'_{10}(j\omega)$ from the iterative procedure (1.48) after 10 iterations. Figure 1.10 shows comparison of the time traces of the solutions of (1.31) obtained by the time domain simulation and by the iterative spectral balance and the inverse Fourier transform. Figure 1.11 shows decay of the power of the approximation error $X'(j\omega) - X'_i(j\omega)$ normalized by the power of $X'(j\omega)$ as a function of iteration step i. Finally, Figure 1.12 shows the contraction rate $\frac{||X'_{i+2}(j\omega) - X'_{i+1}(j\omega)||}{||X'_{i+1}(j\omega) - X'_i(j\omega)||}$ as a function of iteration step i. This verifies the contraction at the rate of about 0.8 was indeed achieved by the loop transofrmation involving solution of the approximate spectral balance.

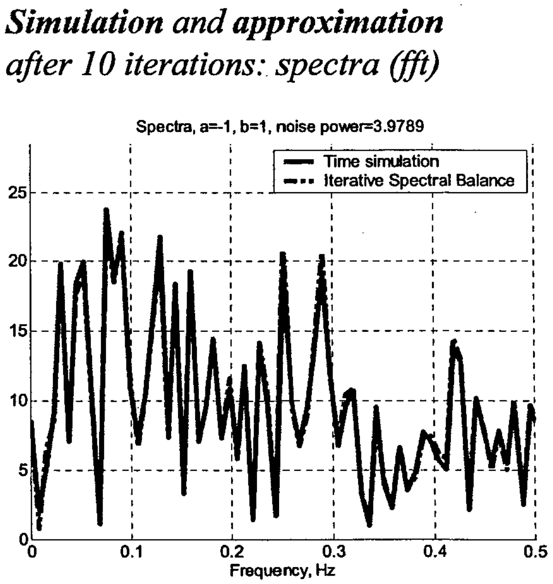

Figure 1.9: Solution to iterative spectral balance equations: spectra

In the cases that were examined obtaining an approximate solution of (1.31) using the formula (1.48) was orders of magnitude faster that the time domain simulations using Simulink.

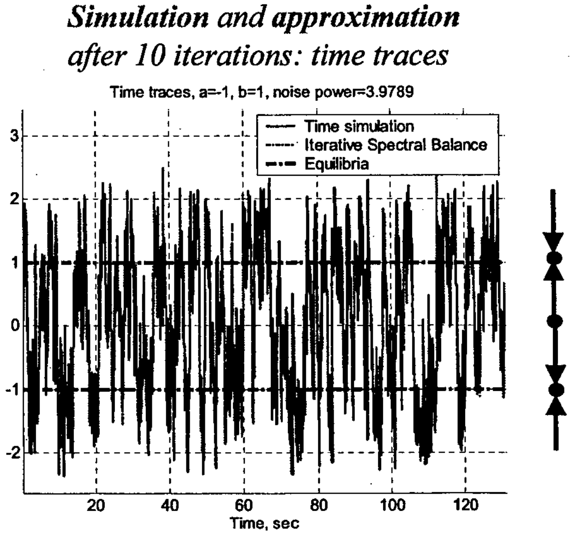

Figure 1.10: Solution to iterative spectral balance equations: time traces

1.2.3 Conclusion

A frequency-domain framework for analysis, computations, and uncertainty propagation in nonlinear systems driven by broad-band disturbances was introduced and illustrated in a simple example of a nonlinear system that exhibits noise-induced transitions between two stable equilibria. The spectral balance framework generalizes the standard harmonic and Gaussian signal balance in feedback systems. The application example presented is a scalar model with cubic nonlinearity after pitchfork bifurcation driven by a broad-band disturbance. An approximate and iterative spectral balance (including determination of equilibria) is solved. The solution of the approximate spectral balance is used to reformulate the original model using a loop transformation so that an iterative procedure for finding the spectrum of the output converges to the true spectrum of the solution. The future work will involve more carefull study of the function spaces suitable for the spectral balance formulation and obtaining some analytic sufficient conditions for the contraction.

1.3 Adaptive Control of Flow Phenomena in Aeroengines

In paper by Banaszuk *et al.*, Automatica 2004, we described adaptive control scheme for control of oscillations with unknown frequency and amplitude and its application to control of thermoacoustic instabilities. The original submission was supported by the previous AFOSR grant, but the subsequent revisions were supported by the current grant.

In paper by Krstic and Banaszuk, Control Engineering Practice 2003, we considered the problem of stabilization of a class of MIMO LTI systems arising in models of various instabilities in jet engines. The problem was motivated by control of flutter, stall, and thermoacoustics in military engines. These instabilities often manifest themselves as oscillations, contaminated by noise. They are often caused by coupling of several resonant modes (structural, acoustic, of vortical) with time delays present in the physical process that couple the resonant modes. Often the control input is also subject to delay. Possible applications of the results in the paper include control of compressor blade flutter, rotating stall, and aeroacoustic instabilities (coupling of acoustic waves with vortex shedding from stator vanes).

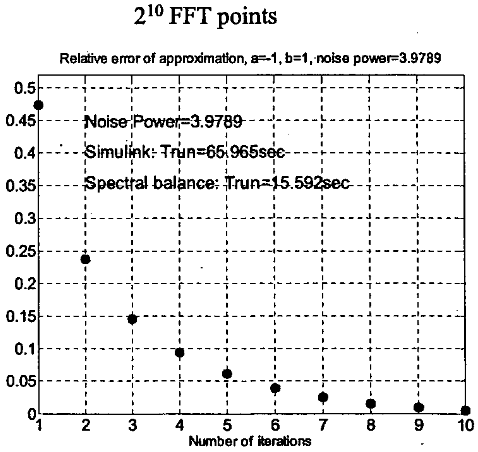

Figure 1.11: Solution to iterative spectral balance equations: relative approximation error for 2^{10} FFT points

Uncertain parameters abound in these problems: unknown or varying natural frequencies, uncertain delays due to poorly understood physical phenomena governing these processes, uncertain coupling between modes of oscillation, and of course, uncertain high frequency gains and delays of actuators. In this paper we approach a class of such models using the tools of adaptive control.

Consider the model of the form

$$\ddot{y}_1 + \xi_{11}\dot{y}_1 + \eta_{11}y_1 + \zeta_{11}y_1(t-\tau_{11}) + \zeta_{12}y_2(t-\tau_{12}) = g_{11}\dot{u}_2(t-\tau_{c,1}) + h_{11}\chi_1 \tag{1.49}$$

$$\ddot{y}_2 + \xi_{22}\dot{y}_2 + \eta_{22}y_2 + \zeta_{22}y_2(t-\tau_{22}) + \zeta_{21}y_1(t-\tau_{21}) = g_{22}\dot{u}_1(t-\tau_{c,2}) + h_{22}\chi_2 \tag{1.50}$$

where y_1 and y_2 are temporal coefficiants of the resonant modes, χ_1 and χ_2 are the disturbance inputs, and the parameters $\xi_{ij}, \eta_{ij}, \zeta_{ij}, \tau_{ij}, g_{ij}, h_{ij}, \tau_{c,i}$ are uncertain. Such a model is common in case where two resonant modes with close resonant frequencies couple though a physical process that involves transport delays. For example, in compressor blade flutter the variables y_1 and y_2 could represent temporal coefficients of blade displacement in a rotating frame. As blades move, they perturb the flow. In turn, the flow perturbations affect (with some delay) the blade motion. Because the blades have airfoil shape and the mean flow has swirl, the flow reponse is not axisymmetric and hence can couple the resonant modes. The cross coupling in the model is represented by the terms $\zeta_{ij}y_i(t-\tau_{ij})$ with $i \neq j$. The terms $\zeta_{ii}y_i(t-\tau_{ii})$ represent effect of flow response on the i-th mode, which can be either stabilizing or destabilizing.

In this paper we were interested in a particular case of strong cross-coupling of identical lightly damped resonant modes represented by the equations

$$\ddot{y}_1 + \eta y_1 + \zeta y_2(t-\tau) = g\dot{u}_2(t-\tau) + h\chi_1 \tag{1.51}$$

$$\ddot{y}_2 + \eta y_2 - \zeta y_1(t-\tau) = -g\dot{u}_1(t-\tau) + h\chi_2. \tag{1.52}$$

Such an interconnection results in coupling of the modes y_1 and y_2. If the latter represent temporal coefficients of resonant standing modes, the coupled dynamics often represents traveling waves. Note that the models of flutter (Banaszuk *et al.*, IFAC 2002) and thermoacoustic instabilities on annular domain (Banaszuk *et al.*, CDC 2003) presented in the later sections of this report are of a similar form.

The adaptive control demonstration in such model is described in details in Krstic and Banaszuk, Control Engineering Practice 2003.

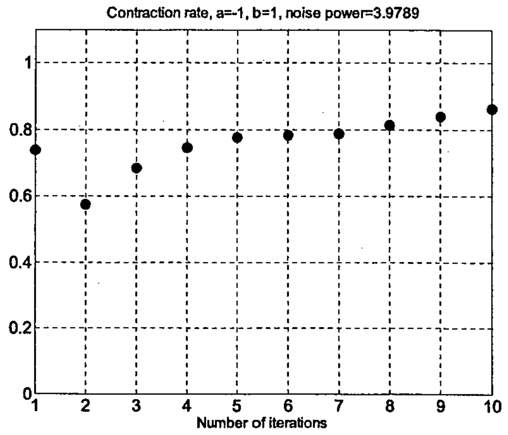

Figure 1.12: Solution to iterative spectral balance equations: contraction rate

1.4 Uncertainty Propagation in Complex, Nonlinear Interconnected Dynamical Systems

Under DARPA funding (AFOSR Contract F49620-03-C-0035) we have shown that the uncertainty propagation in complex, interconnected dynamical systems can be performed more efficiently by decomposing the network based on the hierarchy and/or the strength of coupling. The results of this research are summarized in CDC 2004 papers by Varigonda *et al.*and Huzmezan and Kalmar-Nagy presented in two invited sessions on Uncertainty Propagation. Some basic research aspects of this work were analysed in more detail under the current AFOSR contract. In particular, in Varigonda, CDC 2004, we proposed an iterative method for static feedback systems to obtain the probability density of the output from that of the input. We proved the convergence of the proposed method under the assumption that the loop operator is contractive. The method was illustrated with an example. It was shown, based on the results from the theory iterated random functions, that the method extends to the case when additional parametric uncertainty is present within the loop.

Chapter 2

Control of Flow Phenomena in Military Aeroengines

2.1 Control of Mixing in Shear Flows

2.1.1 Control of Mixing

Papers by Tadmor and Banaszuk, IEEE TCST 2002, Wang *et al.*, Physics of Fluids 2003, and Noack *et al.*, Physics of Fluids 2004 present the results of synergistic use of Control Theory and Dynamical Systems methods to create beneficial, non-equilibrium dynamics in low dimensional fluid models. The common idea is to use control to enforce a periodic behavior in fluid velocity that creates a chaotic advection field for the fuid particles.

2.1.2 Control of Diffuser Flow Separation

In paper by Banaszuk *et al.*, AIAA Reno 2003, we described an application of extremum-seeking to adaptive flow control in a subsonic diffuser. Specifically, we presented results of an experimental study of on-line optimization of the pressure recovery.

Separation phenomena occur in many industrial and military applications including external flows such as flow past high angle of attack airfoils, and internal flows such as aggressively expanding diffusers. Consequently, its control for performance improvement has received widespread attention. Various means for delaying the onset of separation have been proposed, including passive and active methods [19]. The use of periodic oscillations to delay/reduce the extent of separation in airfoils was investigated (e.g. see [50]), demonstrating the effectiveness of unsteady blowing in controlling flow separation. Multi-frequency open loop forcing was shown to create and enhance interactions of multiple flow structures in simple free shear layers [25] Recently, two-frequency forcing using a synthetic jet actuator was shown to be an effective way of increasing diffuser pressure recovery [40]. However, it is difficult to predict an optimal set of parameters that include the number of frequencies, relative amplitude and phase difference between the forcing frequencies for enhancing performance, due to the lack of an analytical or modeling method. In particular, in [40] the parameters for a two-frequency forcing control law that optimized the pressure recovery in a two-dimensional diffuser were found manually.

In this paper we present a method for automatic tuning of parameters of a multi-frequency forcing flow control law to optimize pressure recovery in a diffuser. The method is known in optimization and control theory literature as *extremum seeking* [5] In extremum-seeking control one adapts the control parameters using on-line estimation of gradients of the performance metric with respect to the control paramaters by introducing small probing signals on top of (typically slowly varying) control parameters. The method has been widely applied in industry [49, 1] for "model-free" optimization of steady-state of many industrial processes.

Fore more details we refer to Banaszuk *et al.*, AIAA Reno 2003.

2.1.3 Control of Pattern Factor

Key performance metrics for military aeroengines includes pattern factor, controlled primarily by the combustor stochoimetry and the degree of fuel-air mixing. In a typical non-premixed combustor, both fuel and combustion air are introduced longitudinally at the dump plane, and swirl is generally utilized to mix the fuel and air streams together. In certain combustor designs, additional primary and dilution air are introduced radially through circumferential holes located along the combustor shell. These air-jets in cross flow not only provide the air needed to control the stochiometry, but also generate enhanced fuel-air mixing. Therefore the proper design and utilization of these air-jets can provide a means toward controlling the fuel-air mixing, and enhancing the performance metrics. Increased mixedness, in particular, can provide lower pattern factor.

Control of jets in cross flow was investigated using hierarchy of models (including high fidelity CFD, medium, and low order models) and described in Blossey *et al.*, IUTAM 2001. In particular, low order model-based analysis indicated benefits of low frequency forcing for improved mixing. In the current funding cycle we confirmed the model prediction in experiment. This work is descibed in paper by Narayanan *et al.*, AIAA Journal 2003.

Furthermore, the benefits of jet in cross-flow control for pattern factor reduction were demonstrated in experiment by our academic partners from Luisiana State University. The experiments were not funded by AFOSR. However, the UTRC personnel participation in this joint project was funded by the current AFOSR grant. This work is descibed in detail in Tuncer *et al.*, ASDME 2003. Here we provide a summary of this work.

The effect of a forced dilution air jet introduced through the combustor shell, on the air-fuel mixing in the combustion chamber has been investigated. Thermocouple based temperature measurements have been made at a number of forcing frequencies in the range of 100-1100Hz and blowing ratios in the range of 10-15. The open-loop integral flame response to forcing has also been acquired by recording pressure and heat release spectra. A CH-radical imaging technique is used to provide spatially- and temporally- resolved information about the heat release behavior. The results exhibit that the mean temperature field inside the main reaction zone can significantly be altered as a consequence of air jet modulation. The most significant effects are observed by forcing at vertical locations that are close to the dump plane. Enhancements in temperature of the order of 100–200 degrees C, and reduction in pattern factor of the order of 10% (e.g., from 1.13 to 1.03) were observed, with the lowest pattern factors achieved at the lowest forcing frequency of 100 Hz.

2.2 Modeling, Analysis, and Control of Thermoacoustic Instabilities in Military Engines

In the past, we have considered reduced order models of combustion instability based on lumped parameter modeling as described in [43, 26]. The aim of this Section is to summarize some of the more recent (and ongoing) research whose purpose is to obtain and analyze distributed models of thermoacoustic instabilities in bluffbody flameholder annular combustors. These instabilities arise on account of complicated interactions between combustion (flame and fuel) dynamics, vortex dynamics and acoustics (see Figure 2.1 for a schematic). Our strategy thus far has been to model individual pieces of this inter-connected system with a view of understanding them as a first step towards gaining understanding of the whole. Before summarizing the results, we provide a brief summary of the

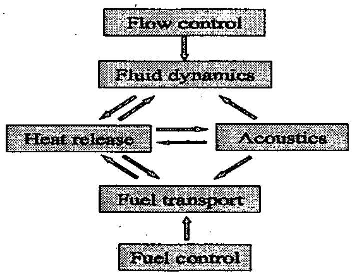

Figure 2.1: Schematic showing interconnection of combustion (flame-fuel), vortex and fuel dynamics in thermoacoustic problem.

modeling activity. There are two areas of modeling: **Thermoacoustic models**, with a view to understand the dynamics of coupled system and **Heat release models**, with a view to understand the combustion and vortex dynamics (sans acoustics). For the thermoacoustic modeling, we have three versions of models which are being studied for the annular combustor problem:

3D Linear model is described in the Section 2.2.1. This model is linear and assumes that dynamics arising due to vorticity and flame motion are neglected. The model allows us to isolate the role of fuel dynamics (shown to be equivalent to a distributed delay for distributed but fixed flame) in analyzing thermoacoustic instabilities. The linearity hypothesis allows us to apply linear (fuel) control methods for controlling rotating wave combustion instabilities in 3D annular combustors. Additional details are provided in Section 2.2.1 and in the paper [32].

2D nonlinear model is described in the Section 2.2.2. In this model, a 3D non-vortical model of thermoacoustic instability is averaged in the radial direction to obtain a 2D model for multiple flameholders. The nonlinearities as well as flame dynamics are retained. The non vortical model is summarized in [33] and is being used for uncertainty analysis and design of so-called *liners* for suppressing combustion instabilities. In Section 2.2.2, a version of this model which includes vorticity by formal superposition of 2D vortex dynamics is summarized.

Single flameholder model is the same as the above 2D nonlinear model (including vorticity and flame dynamics) but the problem is simplified to study only a single flameholder configuration. The details of this model are also summarized in Section 2.2.2.

In addition to thermoacoustic models, we have also concentrated on studying the heat release piece of the thermoacoustic model separately (where acoustics is neglected). There are two reasons for studying the heat release piece. One, the complexity of the thermoacoustic problem resides in the heat release submodel (where complicated interactions occur between flame, fuel and vorticity) and two, fuel and flow control aimed at modifying heat release distribution with a view of controlling combustion instabilities can be studied effectively with these models. Instead of presenting the heat release submodel separately, we describe three studies that have been undertaken with the purpose of analyzing and controlling heat release models. In Section 2.2.3, we present a vortex model developed to study the physics of reacting bluffbody wake dynamics. The model as presented concentrates on the interaction of vorticity and flame dynamics. In the subsequent two Sections, we use reduced order modeling approaches to better understand the reacting flow dynamics and to model other pieces of the heat release model. In particular, in Section 2.2.4 we present a reduced order model study of *flame-fuel* interaction and in Section 2.2.5 a study of *vorticity-flame* interaction (the latter study is carried out to explain some of the results of Section 2.2.3).

2.2.1 Three dimensional linear model

Thermoacoustic instabilities in gas turbine and rocket engines develop when acoustic waves in combustors couple with an unsteady heat release field in a positive feedback loop. We consider an annular combustor that includes a circumferential array of bluff body flame holders [48] [16]. Flameholders extend radially from inner to outer diameter of the annular combustor. A cut along a constant radius surface is shown in Figure 2.2.

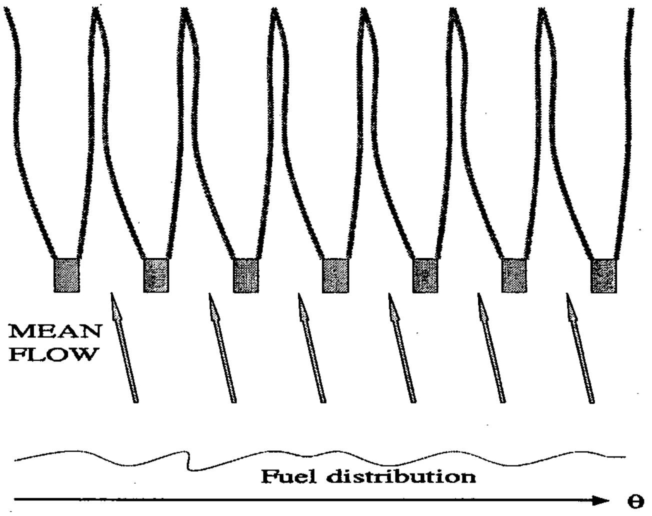

Figure 2.2: Bluff body flameholder array, fuel source surface upstream of flameholders, and flame surface downstream of flameholders.

For the purpose of modeling, we assume that the fuel mass fraction defined at the fuel injection surface $x_0(y,z)$ is advected downstream to the fixed but distributed flame surface $x = g_{fl}(y,z)$ by the sum of the mean and acoustic perturbation velocity (without diffusion). The mean fuel mass fraction at the fuel injection surface is $\overline{Y}_f(x_0,y,z) = \frac{\overline{\chi}_f(x_0,y,z)}{\overline{\chi}_a(x_0,y,z)}$, where $\chi_f = \rho_f U_f$, $\chi_a = \rho_a U_a$ denote the flux and ρ_f, ρ_a are the fuel and air densities and U_f, U_a are the velocities. The perturbation fuel mass fraction (in the presence of acoustics) is

$$y_f(x_0,y,z,t) = \overline{Y}_f(x_0,y,z)\left(\frac{\chi'_f(x_0,y,z,t)}{\overline{\chi}_f(x_0,y,z)} - \frac{\chi'_a(x_0,y,z,t)}{\overline{\chi}_a(x_0,y,z)}\right) \tag{2.1}$$

The fuel-air mixture convects to the fixed flame surface $x = g_{fl}(y,z)$ and the heat release density at the flame surface is obtained as

$$Q(x,y,z,t) \;=\; F_{hr}(Y_f(x,y,z,t))\gamma_{flame}(x - g_{fl}(y,z)), \tag{2.2}$$

where $\gamma_{flame}(\cdot)$ is the axial heat release distribution function representing the flame thickness, and $F_{hr}(\cdot)$ describes local heat release as function of local fuel mass fraction.

In order to obtain the thermoacoustic model, we define relative perturbations of pressure and heat release as $\tilde{p}(x,y,z,t) := \frac{p'(x,y,z,t)}{\gamma\bar{p}(x,y,z)}$ and $\tilde{q}(x,y,z,t) := \frac{\gamma-1}{\gamma}\frac{q'(x,y,z,t)}{\bar{p}(x,y,z)}$, where γ is the ratio of specific heats. We also assume that the acoustic velocity perturbation is purely potential, i.e., $\mathbf{u}'(x,y,z,t) =$

$\nabla\phi(x, y, z, t)$ for some smooth scalar $\phi(x, y, z, t)$ called the *velocity potential.* In these co-ordinates, we obtain a linear distributed thermoacoustic model (see [32] for details) as

$$\frac{\partial}{\partial t}\tilde{p}(x, y, z, t) + \overline{\mathbf{u}}(x, y, z) \cdot \nabla\tilde{p}(x, y, z, t) + \Delta\phi(x, y, z, t) = \tilde{q}(x, y, z, t) \tag{2.3}$$

$$\frac{\partial}{\partial t}\phi(x, y, z, t) + \overline{\mathbf{u}}(x, y, z) \cdot \nabla\phi(x, y, z, t) + a^2\tilde{p}(x, y, z, t) = \eta(x, y, z, t) \tag{2.4}$$

$$\frac{\partial}{\partial t}y_f(x, y, z, t) + \overline{\mathbf{u}}(x, y, z) \cdot \nabla y_f(x, y, z, t) + \nabla\overline{Y}_f(x, y, z) \cdot \nabla\phi(x, y, z, t) = 0 \tag{2.5}$$

$$\tilde{q}(x, y, z, t) = F'_{hr}(\overline{Y}_f(x, y, z))\gamma_{flame}(x - g_{fl}(y, z))y_f(x, y, z, t), \tag{2.6}$$

where driving disturbance (broad-band noise) $\eta(x, y, z, t)$ represents the effect of local turbulence. The fuel mass fraction boundary condition is defined on the fuel injection surface as

$$\frac{y_f(x_0(y, z), y, z, t)}{\overline{Y}_f(x_0(y, z), y, z)} = \left(\frac{u'_f(x_0(y, z), y, z, t)}{\overline{u}_f(x_0(y, z), y, z)} - \frac{1}{\overline{\mathbf{u}}(x_0(y, z), y, z)}\frac{\partial\phi(x_0(y, z), y, z, t)}{\partial x}\right)., \tag{2.7}$$

where the fuel velocity $u'_f(x_0(y, z), y, z, t)$ is the control variable. The first term on the right hand side of (2.7) represents the effect of fuel control action and the second term represents the effect of acoustic velocity perturbation.

The acoustic boundary conditions are provided on the combustor boundary surface in terms of the normal velocity $\mathbf{u}'_n(\mathbf{x}, t) = \nabla\phi(\mathbf{x}, t) \cdot \hat{n}(\mathbf{x})$ (where $\hat{n}(\mathbf{x})$ is the normal vector to the boundary). The acoustic boundary condition serves as another possible control input. We assume that the acoustic boundary conditions are described by a local admittance relation (described here in the frequency domain)

$$U'_n(\mathbf{x}, j\omega) = G^{bc}(\mathbf{x}, j\omega)\tilde{P}(\mathbf{x}, j\omega), \tag{2.8}$$

(see e.g. [39]) for $\mathbf{x} \in \mathcal{S}$, where $\mathcal{S}$ denotes the boundary surface.

Reduced order model for control of thermoacoustic instability on annular domains

The fuel-air mixture is responsible for the burning at the flame and the subsequent heat release. This heat release at the flame surface excites the acoustic waves in the combustor volume. The acoustic waves in turn travel upstream and perturb the transport of the fuel/air mixture. This feedback coupling can lead to instability if the driving resulting from this feedback mechanism dominates the damping resulting from absorption of the acoustic energy at the boundary. Control over fuel rate at the fuel injection surface $x_0(y, z)$, control of the shear layer dynamics using flow control at the flame-holders, or control of the air injection at the combustor boundary can provide ways of influencing the process and eliminating instability. The control could be provided at various temporal and spatial scales.

Now we introduce a reduced order model (that is suitable for control design) obtained from the thermoacoustic instability model presented above. The model is also suitable for optimization of the control architecture. In order to obtain model reduction, we expand the pressure and potential perturbations in terms of the acoustic modes $\{\Pi_k(\mathbf{x})\}_{k=1,2,\ldots}$ as $\tilde{p}(\mathbf{x}, t) = \sum_k p_k(t)\Pi_k(\mathbf{x})$, $\phi(\mathbf{x}, t) = \sum_k \phi_k(t)\Pi_k(\mathbf{x})$. and apply standard Galerkin procedure involving integration by parts and using the admittance condition (2.8) (see [32] for details) to obtain a two mode model represented in the frequency domain as

$$j\omega\begin{bmatrix}\Phi_1(j\omega)\\ \Phi_2(j\omega)\\ P_1(j\omega)\\ P_2(j\omega)\end{bmatrix} = \begin{bmatrix}0 & 0 & -a^2 & 0\\ 0 & 0 & 0 & -a^2\\ \lambda_1 & 0 & 0 & 0\\ 0 & \lambda_2 & 0 & 0\end{bmatrix}\begin{bmatrix}\Phi_1(j\omega)\\ \Phi_2(j\omega)\\ P_1(j\omega)\\ P_2(j\omega)\end{bmatrix} + \begin{bmatrix}N_1(j\omega)\\ N_2(j\omega)\\ Q_1(j\omega) - V_1(j\omega)\\ Q_2(j\omega) - V_2(j\omega)\end{bmatrix}, \tag{2.9}$$

where $Q_m(j\omega)$, $N_m(j\omega)$, and $V_m(j\omega)$, denote the Fourier transforms of

$$q_m(t) = \int_{\mathcal{V}} \Pi_m(\mathbf{x})\tilde{\mathbf{q}}(\mathbf{x},\mathbf{t})\mathbf{dx}, \tag{2.10}$$

$$\eta_m(t) = \int_{\mathcal{V}} \Pi_m(\mathbf{x})\tilde{\eta}(\mathbf{x},\mathbf{t})\mathbf{dx}, \tag{2.11}$$

$$v_m(t) = \int_{\mathcal{S}} \Pi_m(\mathbf{x})\mathbf{u}'_{\mathbf{n}}(\mathbf{x},\mathbf{t})\mathbf{dx}, \tag{2.12}$$

respectively, and $\lambda_m := \frac{\int_{\mathcal{V}} |\nabla\Pi_m(\mathbf{x})|^2 \mathbf{dx}}{\int_{\mathcal{V}} |\Pi_m(\mathbf{x})|^2 \mathbf{dx}}$ ($\mathcal{V}$ and $\mathcal{S}$ denotes the combustor volume and boundary surface respectively). The fuel velocity $u'_f(x_0(y,z),y,z,t)$ at the fuel injection surface is the control variable. We assume that the control is realized using N_{inj} fuel injectors with $i-th$ fuel injector providing fuel mass flux equal $w_{f,i}(t)$ with spatial distribution $k_{f,i}(y,z)$ (representing initial fuel spread in the direction perpendicular to the mean flow). Thus, we will represent the distributed velocity as $u'_f(x_0(y,z),y,z,t) = \sum_{i=1}^{N_{inj}} k_{f,i}(y,z)w_{f,i}(t)$, with $w_{f,i}(t)$ representing the control inputs.

The closure equations to (2.9) are given by

$$V_m(j\omega) = G_m^{bc}(j\omega)P_m(j\omega) \tag{2.13}$$

$$Q_m(j\omega) = \sum_{k=1}^{2} G_{mk}^{\phi 2q}(j\omega)\Phi_m(j\omega) + \sum_{i=1}^{N_{inj}} G_{mi}^{u_f 2q}(j\omega)W_{f,i}(j\omega). \tag{2.14}$$

The transfer functions in the above expression have the form

$$G_m^{bc}(j\omega) := \int_{\mathcal{S}} G^{bc}(\mathbf{x},j\omega)|\Pi_m(\mathbf{x})|^2 d\mathbf{x} \tag{2.15}$$

$$G_{mk}^{\phi 2q}(j\omega) = \int_{\mathcal{W}} \frac{-1}{\overline{u}(y,z)}\Pi_m(g_{fl}(y,z),y,z)F'(\overline{Y}_f(y,z))\nabla\overline{Y}_f(y,z)\nabla\Pi_k(x,y,z)e^{-j\omega\frac{g_{fl}(y,z)-x}{\overline{u}(y,z)}}dxdydz \tag{2.16}$$

$$G_{mi}^{u_f 2q}(j\omega) = \int_{x_0} \frac{k_{f,i}(y,z)}{\overline{u}_f(x_0(y,z),y,z)}\Pi_m(g_{fl}(y,z),y,z)F'(\overline{Y}_f(y,z))e^{-j\omega\frac{g_{fl}(y,z)-x_0(y,z)}{\overline{u}(y,z)}}dydz \tag{2.17}$$

While the reduced order frequency domain model looks deceivingly simple, it is in fact a complicated infinite dimensional model, as the heat release response transfer functions include a distributed delay.

We assume that pressure measurements $\tilde{p}(\mathbf{x}_i,t) = \sum_k p_k(t)\Pi_k(\mathbf{x}_i)$ at one or several locations $\mathbf{x}_i$ are available. We also assume that disturbance terms $N_1(j\omega)$, $N_2(j\omega)$ are broad band uncorrelated stochastic processes. The objective of the feedback control is to reduce the gain ($\mathcal{H}_\infty$ or $\mathcal{H}_2$) from the disturbance terms N_1, N_2 to the pressure terms P_1, P_2 to guarantee that the pressure level is below acceptable level. Once the mean fuel mass fraction distribution $\overline{Y}_f(y,z)$ and control fuel injection (represented by choice of influence functions $k_{f,i}(y,z)$) are defined, linear control laws are straightforward to obtain. However, the real challenge is *optimization of the control architecture.* Namely, one would like to select the mean fuel mass fraction distribution $\overline{Y}_f(y,z)$ and control fuel injection influence functions $k_{f,i}(y,z)$ that guarantees meeting the control objective with minimal amount of fuel used for control.

2.2.2 Two dimensional nonlinear model

Thermoacoustics models incorporating effects of distributed acoustics, flame dynamics and vorticity in bluffbody flameholder annular combustors have been developed. In this Section, we first describe a 2D nonlinear model without vorticity that is intended for liner design. Details on this model can be found in [33], where first a 3D model is obtained and then averaging along the radial direction yields a 2D version of the model. The linearized potential acoustics for this model are described by

$$\begin{aligned}\frac{\partial p}{\partial t} + \underline{U} \cdot \nabla p + \gamma \mu S_T[\bar{Y}_f]\delta(\underline{x} - \underline{\bar{x}}_f)p - \rho_0 \frac{1}{2}\nabla|\underline{U}|^2 \cdot \nabla\phi & \\ + \rho_0 c^2 \Delta\phi + \left.\frac{\partial \phi_a}{\partial r}\right|_{R_1}^{R_2} &= (\gamma - 1)q, \qquad (2.18)\\ \frac{\partial \phi}{\partial t} + \underline{U} \cdot \nabla\phi &= -\frac{p}{\rho_0}, \qquad (2.19)\end{aligned}$$

where ϕ, p denote the averaged 2D acoustic potential and pressure respectively, $\underline{U}$ denotes the mean flow, S_T is the flame speed, a function of mean local fuel mass fraction $\bar{Y}_f$, the term $\frac{\partial \phi_a}{\partial r}\Big|_{R_1}^{R_2}$ arises on account of the radial boundary conditions and model the effect of liner (wall normal velocity), and parameters ρ_0, γ, c denote fluid density, ratio of specific heats, speed of sound respectively and the parameter $\mu = (\frac{\rho_u}{\rho_b} - 1)$. q represents the heat release perturbation, which arises due to the flame dynamics modeled by G-equations describing the motion of individual flames

$$\frac{\partial G}{\partial t} + [\underline{U} + \nabla\phi] \cdot \nabla G + S_T|\nabla G| = 0, \qquad (2.20)$$

where the flame speed S_T is determined from the solution of the fuel advection equation, written in 2D as

$$\frac{\partial Y_f}{\partial t} + (\underline{U} + \nabla\phi) \cdot \nabla Y_f = 0. \qquad (2.21)$$

The boundary conditions arise due to the acoustic boundary condition at the flameholder walls

$$\nabla\phi \cdot \hat{n}_w|_{\text{Flameholder Walls}} = 0, \qquad (2.22)$$

and the inlet fuel profile

$$Y_f^0 = \frac{\rho_f U_f}{(\rho_0 + \frac{p}{c^2})(U + \frac{\partial \phi}{\partial x})}, \qquad (2.23)$$

where $\rho_f U_f$ denotes the fuel mass flux and U denotes the axial component of flow velocity.

In [33], we present the above model for describing combustion instabilities in annular combustors. The model is being used to study robust linear design, where the control input acts through the boundary liner terms $\frac{\partial \phi_a}{\partial r}\Big|_{R_1}^{R_2}$ in the acoustic model above. The model includes a model for mean flow

$$\underline{U} = \underline{U}_p + \underline{U}_e, \qquad (2.24)$$

where the potential flows $\underline{U}_p$ models the inflow of reactants and $\underline{U}_e$ models the expansion velocity created because of burning, arises as a solution to the continuity equation

$$\nabla \cdot \underline{U}_e = -\frac{1}{\rho}\frac{D\rho}{Dt}, \qquad (2.25)$$

together with appropriate boundary conditions (see [33] for details on the model). An example of the above model with only a single flameholder (see Figure 2.3 for schematic) is explicitly constructed and presented in the report.

Our preliminary attempt at extending the model to include vortex dynamics is to use the decomposition of velocity field similar to equation (2.24) above but now include a term due to vorticity

$$\underline{U} = \underline{U}_p + \underline{U}_e + \underline{U}_\omega, \qquad (2.26)$$

where vortical velocity arises as a solution of the vorticity equation

$$\frac{\partial \omega}{\partial t} + ([\underline{U} + \nabla\phi] \cdot \nabla)\omega + (\nabla \cdot \underline{U} + \Delta\phi)\omega = \frac{1}{Re}\Delta\omega + \frac{1}{\rho^2}\nabla\rho \times \nabla P. \qquad (2.27)$$

Rigorous justification of the above extension is part of the ongoing research.

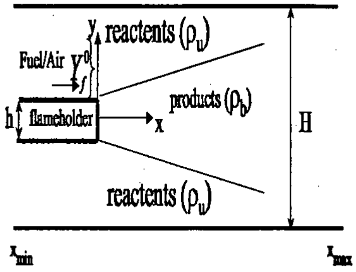

Figure 2.3: Schematic of the physical problem.

2.2.3 FLAVOR - A vortex model for reacting flow bluffbody wake dynamics

In our paper [36], we present a vortex model for bluff body flameholder stabilized premixed combustion. We consider the physical problem of non-premixed combustion stabilized by a single rectangular bluff body flameholder of height h in a channel of height H (see Figure 2.3 for a schematic). The size of both the bluff body and the channel in the third dimension (z) is large so that two-dimensionality is assumed to apply. The Mach number is low and both reactants (of density ρ_u) and products (of density ρ_b) are assumed to behave as ideal gases. The combustion time scale is much faster than that of the flow and the reacting field is assumed to be approximated by two flamesheets anchored at the two flameholder lips.

The evolution of the flow is governed by the vorticity and continuity equations

$$\frac{\partial \omega}{\partial t} + (\underline{u} \cdot \nabla)\omega + (\nabla \cdot \underline{u})\omega = \frac{1}{Re}\Delta\omega + \frac{1}{\rho^2}\nabla\rho \times \nabla p, \tag{2.28}$$

$$\nabla \cdot \underline{u} = -\frac{1}{\rho}\frac{D\rho}{Dt} \tag{2.29}$$

together with the no-slip and impermiability boundary conditions at the flameholder walls and impermiability boundary conditions at the channel walls. A G-equation formulation (see [27]) is used to describe the flame evolution as

$$\frac{\partial G}{\partial t} + ([\underline{u} + S_T(\underline{x}_f)\hat{n}].\nabla)G = 0, \tag{2.30}$$

where the flamesheet is described by the (unidimensional) connected locus of the points $\underline{x}_f$ satisfying $G(\underline{x}_f, t) = 0$ and $\hat{n}$ is the unit normal to the flame oriented into reactants. For the premixed case considered here, the flame speed is modeled to be its stoichiometric value, while retaining the effects of curvature (using Markstein length).

The Lagrangian Vortex Element Method (VEM) in the form that accommodates the presence of reaction in the low Mach number limit [22] is used to reproduce the unsteady flow. The Lagrangian implementation of the flamesheet evolution is performed using numerical techniques consistent with the VEM. The numerical model is validated against non-reacting experimental data for shear layers (results included in [14]) simulated by considering a thin bluff body with a velocity difference across it - and traditional bluff body flows [44]. The results of this validation is presented in our paper [36].

Results for the reacting bluff body flow indicate a shift in the solution from the Von Karman asymmetric shedding of coherent vortices at a characteristic frequency witnessed in the non-reacting flow, to a rather symmetric shedding that is not dominated by any single frequency. Figure 2.4 contrasts the time-series and frequency spectra, based on the v-velocity signal taken on the centerline half bluff body width downstream of the bluff body trailing edge, for the reacting and non-reacting cases. The reduction in unsteadiness (with respect to the non-reacting case) seen in the figure is consistent with

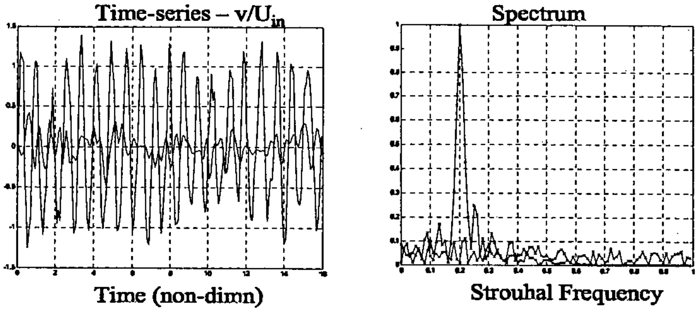

(a) (b)

Figure 2.4: (a) Time series and (b) spectral plots of the non-reacting (blue) and reacting (red) v-velocity signal on the centerline (y=0) at half a bluff body width downstream from trailing edge.

the experimentally obtained spectral plots, comparing non-reacting and reacting spectra, presented in [47]. Analysis presented in our paper [36] indicates that this shift is mainly due to the dilatation that accompanies the combustion heat release while baroclinic vorticity plays a supporting but secondary role. The dynamics in the near field of the flameholder (4-5 bluff body thickness downstream) is dominated by the vorticity generated at the bluff body walls. The dilatation weakens this wall generated vorticity as it goes through the flame and delays the entrainment of some of this vorticity into the products region of the wake. Both effects tend to diminish the interaction of the opposite signed vorticity emerging from the boundary layers on the two horizontal bluff body walls, thereby diminishing the possibility of a Von Karman street. Further downstream vorticity generated by the baroclinic torque dominates the dynamics. The amount of the downstream baroclinic vorticity is strongly dependent on the presence of wall generated vorticity. The latter excites the flame in the near field thereby enhancing the conditions for baroclinic vorticity generation. Characteristic simulation results are shown in Figure 2.5.

2.2.4 Reduced order modeling for *Control*

Fuel control is a viable strategy for suppressing the combustion instability induced pressure oscillations. However, the application of fuel control to bluffbody environment with its distributed fluid dynamics, combustion and acoustics is yet to be done. In the following subsection, we present the past research whose explicit aim was to apply reduced order modeling for the purpose of investigating control.

A primary difficulty in applying fuel control to bluffbody flameholders arises due to the lack of suitable reduced order models that can be used for control design. In some of the past research at UTRC, we made a simplifying assumption of neglecting the effect of vortical dynamics to obtain reduced order models, which we used for studying fundamental limitations on control design. The control was demonstrated on the full computational model. Below we provide a summary of this research; see [34] for details.

We consider the physical problem described above in Section 2.2.3 and in figure 2.3. The primary difference here is that while the flow is simplified (by neglecting vortex dynamics), combustion now is assumed to be non-premixed (so additional equations are needed to describe the evolution of fuel). For the purpose of modeling and controlling combustion instability, we are primarily interested in the spatio-temporal distribution of the heat release response $q(\underline{x},t)$ which is function of local flame speed and the flame location

$$q(\underline{x},t) \propto S_T(\underline{x}_f)\delta(\underline{x}-\underline{x}_f). \tag{2.31}$$

The flame dynamics arise due to (complicated) interaction between the fluid dynamics and the

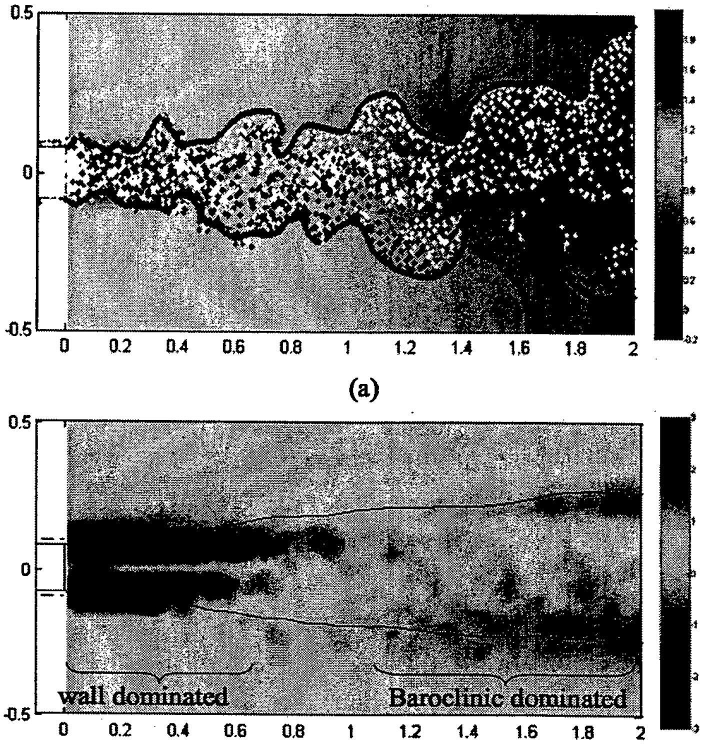

(a)

(b)

Figure 2.5: Flow visualization of the reacting flow with h/H=0.16, h/H=20, Re=20000, and . (a) Instantaneous flame location (lines), center of vortex elements (black/white points denoting -/+ signed vorticity) together with the mean streamwise velocity field (shades). (b). Mean flame location (lines) together with mean vorticity (shades) - the color axis range for vorticity plot is chopped to better view the weaker baroclinic vorticity.

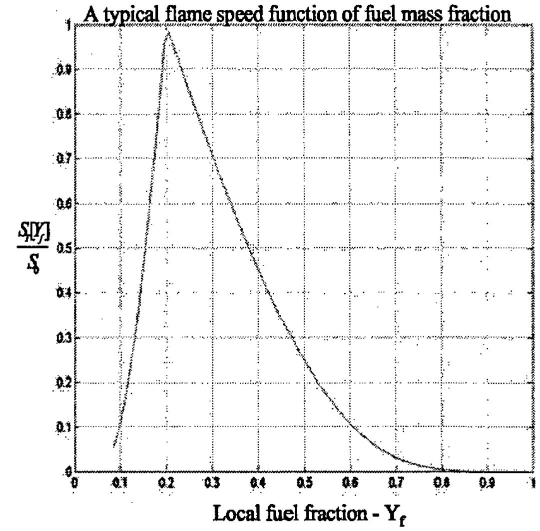

Figure 2.6: Plot of a typical flame speed function $S_T[Y_f]$: the peak corresponds to stoichiometric condition where the flame burns with maximal flame speed S_0.

inherent kinematic flame motion. The 2D nature of the problem, boundary conditions and bluffbody geometry (where there are no translation symmetries) makes reduced order modeling for the purpose of understanding and controlling the reacting flow problem difficult. We make a simplifying assumption of ignoring the vortical component of the fluid dynamics in the problem, but retain the effects due to burning and fuel actuation. The equations of flow retain the continuity equation but the vorticity equation is now replaced with

$$\nabla \times \underline{u} = 0, \tag{2.32}$$

and for the boundary conditions, only the impermiability condition is retained (the no-slip condition is dropped). The G-equation is once again used to describe the flame motion but now for the non-premixed case, the flame speed

$$S_T(\underline{x}_f) = S_T[Y_f(\underline{x}_f)] \tag{2.33}$$

is a function of the local fuel mass fraction for the non-premixed situation considered here. Figure 2.6 plots a typical $S_T[Y_f]$ as a function of Y_f. We reserve the square bracket notation $S_T[\cdot]$ for the function to distinguish it from the flame speed S_T. The local fuel mass fraction seen at the flame front arises due to the convection of the fuel-air mixture in the duct

$$\frac{DY_f}{Dt} = 0. \tag{2.34}$$

An initial upstream profile

$$Y_f(x = 0, y, t) = Y_f^0(y, t) \tag{2.35}$$

provides a boundary condition at the entrance of each of the half channels upstream (on either side) of the bluff body (see Figure 2.3). This initial distribution convects with the flow velocity (because of (2.34)) until it burns at the flame front. Here, we assume that the fuel distribution is such that a lean condition (where the fuel mass fraction Y_F is less than the stoichiometric value- see Figure 2.6) always applies. As a result, *all* of the fuel is burnt at the flame and the flame provides an appropriate second boundary condition for (2.34).

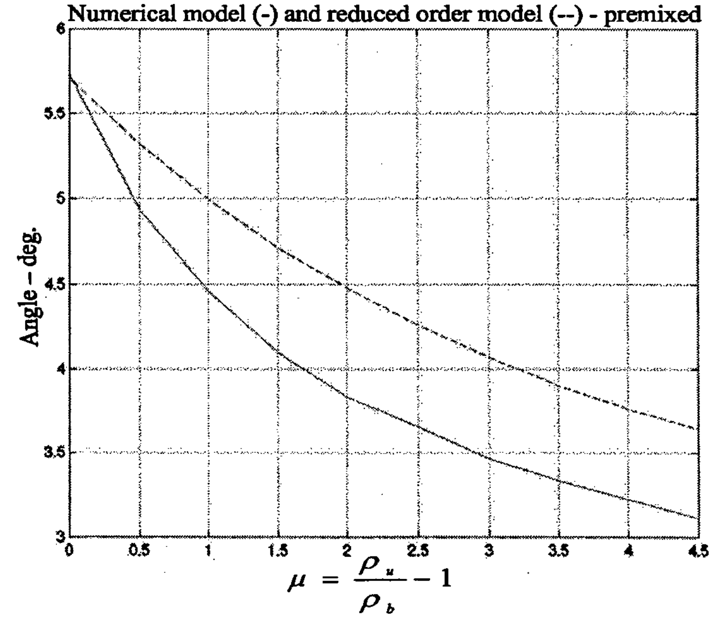

Figure 2.7: Plot showing shallowing of flame angle as density ratio increases: the difference between numerical model (-) and reduced order model (dashed) is less than 0.5 degrees even for large density ratios.

We derive a reduced order model for the individual flame motion as

$$\begin{aligned} \frac{\partial \xi}{\partial t} + \left\{ S_T \left[Y_f^0(y, t - \frac{\xi}{U_0}) \right] + \frac{\mu}{H} S_T^0 (\frac{H}{2} - 2y) \right\} \frac{\partial \xi}{\partial y} &= U_0 + \frac{\mu}{H} S_T^0 \xi && (2.36) \\ \xi(y = 0, t) &= 0, && (2.37) \\ \xi(y, t = 0) &= \xi^0, && (2.38) \end{aligned}$$

a hyperbolic initial boundary value problem (IBVP) - here $(\xi(y,t), y)$ denote the co-ordinate of the flame location. Here $\mu = (\frac{\rho_u}{\rho_b} - 1)$, where ρ_u is the density of the unburnt reactants and ρ_b is the density of the products.

We also validated the reduced order model against the simulation results of a CFD numerical model. The reduced order model was shown to accurately reproduce both the flame shapes and flame angles as a function of density ratio parameter μ for premixed flames (see Figure 2.7) and accurately predict the flame blowoff seen in the computational model for the non-premixed case as the fuel penetration into the cross-stream increases (see Figure 2.8).

We also used the reduced order model to define and study a (fuel actuation based) control problem of tracking the heat released due to flame motion against a prescribed reference signal (for the full simulation). The problem is motivated by the problem of fuel control of combustion instability. In order to completely address the issue of control authority needed to quench pressure oscillations in combustor to an acceptable level, one needs to investigate the coupled acoustic-flame system model [32]. In the paper, however, we concentrated on controlling the distributed heat release response by manipulating the inlet fuel profile (see Figure 2.9 for a schematic of the control problem). A heuristic interpretation for considering this *piece* of the problem is provided in [34]. For the control problem described in the figure, we proposed an optimal control strategy which was then implemented on the computational model to track the heat released against a prescribed reference signal. Figure 2.10 provides a comparison of the tracking signal against the heat release obtained from the simulation.

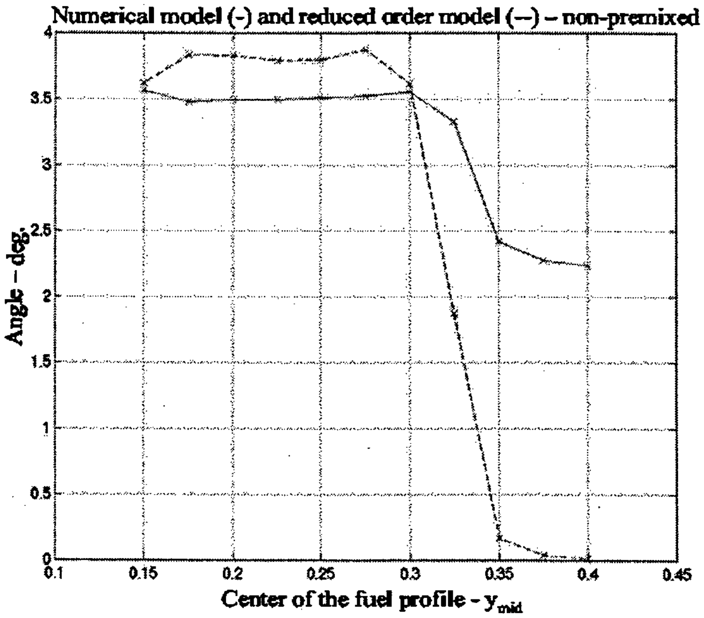

Figure 2.8: Flame angle as fuel center y_{mid} (defines the inlet fuel profile as $Y_f^0(y) = \frac{C_0}{\sqrt{2\pi}\sigma} e^{\frac{(y-y_{mid})^2}{\sigma^2}}$) varies: model captures the critical value of flame blow-off as well as flame angles for robust flame before blow-off.

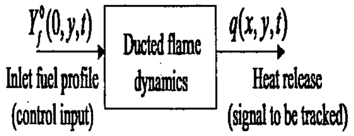

Figure 2.9: Schematic of the control problem.

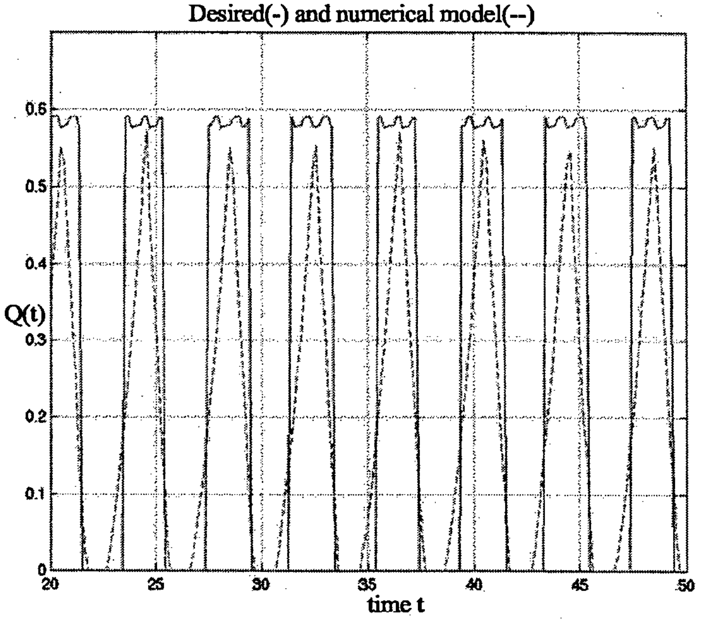

Figure 2.10: Results of the implementing the tracking control on the numerical model.

Analysis of the control was provided in the paper and suggested in a fundamental limitation associated with ON-OFF control of heat release. This limitation is suggested in Figure 2.10 as discrepancy between the desired and the controlled heat release response. The limitation arises due to the hyperbolic nature of the problem which leads to solution discontinuities with ON-OFF control; complete analysis using method of characteristics is provided in [34].

2.2.5 Reduced order modeling for *Dynamic range analysis*

The occurrence of combustion instability in augmentors using bluffbody flameholders is a function of the operating conditions [8]. Dynamic range analysis is important not only to map the stability boundaries (where instabilities occur) and predict post instability response (for instance, the pressure amplitudes) but also to identify the important physical mechanisms that lead to the instabilities as a function of parameters in the problem. There are two challenges associated with meeting the objective

1. The computational cost associated with mapping out all the different regimes of physical phenomenon is prohibitive,
2. Even if a transition of physical phenomenon is seen in the computational model, an understanding of key physical mechanisms underlying this transition is difficult to obtain because of the distributed and nonlinear nature of the dynamics.

For the purpose of reducing the computational burden, we are interested in model reduction approaches that can model the computationally expensive elements (such as vortex dynamics) in reduced order fashion. In the following subsection, we summarize one such approach - a Galerkin based reduced order modeling framework - used to understand the suppression of Von Karman vortex shedding for compressible reacting flows. This ongoing work is as yet unpublished, but available as a preprint [35].

The wake dynamics of a bluffbody stabilized reacting flows are very different from their non-reacting counterpart. In particular, while a Von Karman asymmetric shedding of coherent vortices at a characteristic frequency is witnessed in the non-reacting flow, reacting flows exhibit a rather symmetric shedding that is not dominated by any single frequency (see our recent computational paper [36], also the review paper [10], computational papers of [9] and [41] and experiments of [47]). A variety of explanations have been proposed in the literature, the majority of them pointing to the vorticity generated by the flame via the baroclinic mechanism as the primary reason behind the exhibited shift in flow behavior. For example, [10] attributes the shift to the combination of two possible mechanisms: (i) the dampening of the vorticity due to the increased kinematic viscosity of the reacted fluid and, (ii) the generation of baroclinic vorticity that is of opposite sign to the flameholder generated vorticity and tends to nullify the effects of the latter. Menon and co- workers also point to the baroclinic vorticity generation as the main mechanism that leads to the shift [9]. In our own paper [36], we argue the importance of exothermic effects in suppressing the Von Karman shedding observed in cold bluffbody flow.

In our more recent work, we use Galerkin based reduced order models for investigating the effect of exothermicity on reacting bluffbody flows. In particular, we are interested in explaining (within the reduced order models) the suppression of Von Karman shedding in the presence of burning. In order to obtain model reduction, our approach is to reduce the order of the fluid dynamics using (Noack-Tadmor [21]) inspired) POD based Galerkin model. To obtain the Galerkin model, we begin with the compressible form of vorticity equation

$$\frac{\partial \omega}{\partial t} + (\underline{u} \cdot \nabla)\omega + (\nabla \cdot \underline{u})\omega = \frac{1}{Re}\Delta\omega + \frac{1}{\rho^2}\nabla\rho \times \nabla p. \tag{2.39}$$

We make a simplifying assumption of ignoring the effect of baroclinicity,

$$\frac{1}{\rho}\nabla\rho \times \nabla p = 0, \tag{2.40}$$

which is motivated by some of the results summarized in [36], where we have argued the importance of exothermicity ($\nabla \cdot \underline{u} \geq 0$) in obtaining suppression.

In [35], we show that the reduced order Galerkin model (with three POD modes) has the following structure

$$\begin{aligned}
\frac{d}{dt}\begin{bmatrix} \omega_\Delta \\ \omega_1 \\ \omega_2 \end{bmatrix} &= \begin{bmatrix} -\rho & -\delta\omega_1 & -\delta\omega_2 \\ \delta\omega_1 & \alpha & -\omega \\ \delta\omega_2 & \omega & \alpha \end{bmatrix}\begin{bmatrix} \omega_\Delta \\ \omega_1 \\ \omega_2 \end{bmatrix} \\
&+\mu\left\{\begin{bmatrix} \gamma_\Delta & 0 & 0 \\ 0 & \gamma & -\omega_b \\ 0 & \omega_c & \gamma \end{bmatrix} + \begin{bmatrix} -\beta_\Delta & 0 & 0 \\ 0 & -\beta & 0 \\ 0 & 0 & -\beta \end{bmatrix}\right\}\begin{bmatrix} \omega_\Delta \\ \omega_1 \\ \omega_2 \end{bmatrix},
\end{aligned} \tag{2.41}$$

where $(\omega_\Delta, \omega_1, \omega_2)$ are the modal coefficients, the first term on the right hand side of equation (2.41) models the non-reacting wake flow dynamics (see [21] for their physical significance) and the second and third terms model the effect of burning (recall $\mu = (\frac{\rho_u}{\rho_b} - 1)$). The second term models the effect of exothermicity captured by the compressible term $(\nabla \cdot \underline{u})\omega$ in the vorticity equation (2.39). The third term models the effect of convection because of the dilatation flow (arises as a component of the term $(\underline{u} \cdot \nabla)\omega$ in the vorticity equation (2.39)) which causes the vorticity to convect differently than for a non-reacting flow.

In the absence of burning, the 3 mode Galerkin model reproduces the sequence of bifurcations from fully attached steady flow to a steady flow with symmetric recirculation regions in the wake to an assymetric Von Karman shedding solution (see Figure 2.11). In the reduced order model, the effect of the burning is to laminarize the flow by moving the Hopf bifurcation point corresponding to the appearance of Von Karman shedding solution to higher Reynolds numbers. Furthermore, beyond a critical value of parameter ($\mu \approx 1.4$), the shedding solution dissapears for all values of Reynolds

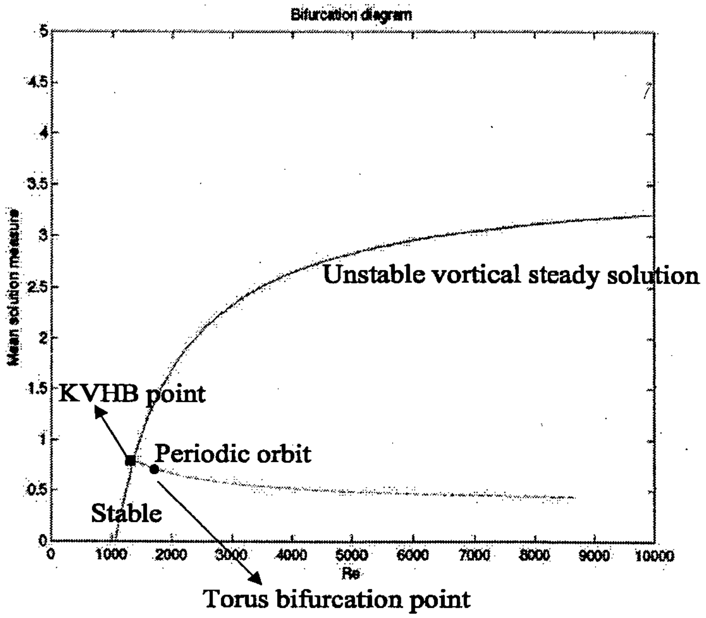

Figure 2.11: Bifurcation diagram for the Galerkin model

numbers (see Figure 2.12 for a locus of Hopf bifurcation point as a function of the two parameters - Reynolds number Re and μ). The value of $\mu = 1.4$ is in a nice agreement with our reported value for disappearance of Von Karman shedding solution for high Reynolds number flows [36].

2.3 Passive control of thermoacoustic instabilities by symmetry-breaking

In paper by Hagen and Banaszuk, CDC 2004, we presented a thermo-acoustic model on a cylindrical, or annular, geometry, capable of modeling instabilities of tangential acoustic modes. The model accounts for non-uniform density, damping, rotational flow, and heat-release coupling. It is shown that deliberately introducing spatial variations in some quantities has a similar effect to adding damping to the system. The effects of these symmetry-breaking conceptes are evaluated on the model through linear analysis and the net amount of additional damping is computed. We showed how various symmetry-breaking concepts are robust with respect to the uncertainty in the model parameters and we examined propagation of uncertainty with respect to a measure of uncertainty recently defined by I. Mezic.

2.4 Background noise effect on combustor stability

Paper by Lieuwen and Banaszuk, Journal of Propulsion and Power 2004, considers the effects of background turbulent fluctuations upon a combustor's stability boundaries. Inherent turbulent fluctuations act as both additive and parametric excitation sources to acoustic waves in combustors. While additive noise sources exert primarily quantitative effects upon combustor oscillations, parametric noise sources can exert qualitative impacts upon its dynamics; particularly of interest here is their ability to destabilize a system that is stable in the absence of these noise sources. The significance of these parametric noise sources increases with increased background noise levels and, thus, may play more of

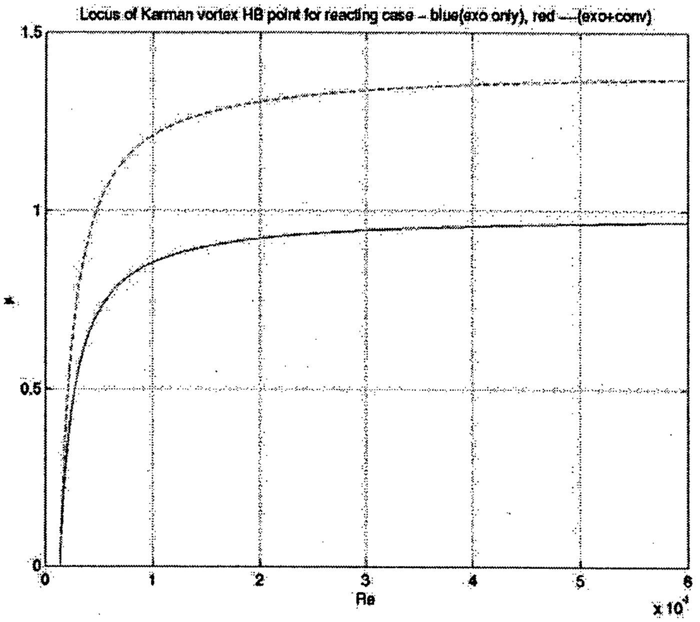

Figure 2.12: Locus of Hopf bifurcation point in Re-μ plane: The Hopf point denoting the Reynolds number where the Von Karman vortex shedding solution begins is moved out to its inviscid limit as μ increases to ≈ 1.4.

a role in realistic, high Reynolds number systems than experiments on simplified, lab scale combustors might suggest. The objective of this paper is to determine whether and/or when these effects might be significant. The analysis considers the effects of fluctuations in damping rate, frequency and combustion response. It is found that the effects of noisy damping and frequency upon the combustor's stability limits is relatively small, at least for the fluctuation intensities estimated here. The effects of a noisy combustion response, particularly of a fluctuating time delay between flow and heat release perturbations, can be quite significant, however, in some cases for turbulence intensities as low as 5-10%. These results suggest that deterministic stability models calibrated on low turbulence intensity, lab scale combustors may not adequately describe the stability limits of realistic, highly turbulent combustors.

2.5 Modeling, Analysis, and Control of Flutter in Turbomachinery

A linear framework for control of wave phenomena on annular domain was established. The flutter control problem was used to motivate the study. However, the framework applies to control of general wave phenomena on annular domain, such as rotating stall and thermoacoustic instabilities.

In papers by Banaszuk *et al.*, IFAC 2002, CDC 2002, AIAA 2003, we described a method for controlling fan or compressor blades flutter in gas turbine engines and its experimental demonstration. The experimental implementation of active flutter control on a sub-scale fan rig consisted of an array of audio speaker-powered volumetric sources connected to the flow path equally spaced along the circumference axially located between an experimental fan and its exit guide vanes (stator). Blade arrival time detectors based on eddy current sensors placed at the leading end of the blade-tip line were used to generate real-time blade deflection signals. An observer was used to reconstruct the flutter modes. A pole-placement controller was used to generate the speaker command signals. The control system was able to add significant amount of damping to three modes of flutter. Damping augmentation was an order of magnitude larger than the intrinsic aeromechanical damping of the modes on the operating line of the fan.

Blade failures due to flow induced vibrations are a long standing, endemic problem for the turbomachinery industry. Flutter and resonant stress fundamentally constrain the design and operation of gas turbine engines. Ensuring aeromechanical operability often requires compromises in turbomachine efficiency, performance and cost and can result in development delays and increased mainatinance costs.

We describe a method for controlling fan and compressor balde flutter in gas turbine engines, as well as a particular implementation of this approach demonstrated in experiments in a transsonic fan rig operating at 9000 RPM. The limitations in operability of a turbomachine due to flutter can be overcome by adding damping to the dominant aeromechanical modes.

We model the dynamics of blade rows in turbo-machinery as similar to those of a flexible disk. Aeromechanical modes form travelling waves as seen by the rotor. This means that when viewed from the rotating frame the peak of deflection appears to travel around the disk. The deflection of the disk at a given point on the fixed frame along the circumference of the blade-row can be decomposed into sinusoids of frequencies separated by integer multiples of the rotor frequency. At any fixed point in time, the deflection of the disk can also be decomposed into sine-waves function of the angular position around the rotor. Therefore each aeromechanical mode has a characteristic shape and a characteristic frequency. Each of these modes can lose stability as operating conditions change. The objective of a flutter control is to enhance the region of stable operation by adding damping to the aeromechanical modes.

The preferred sensing scheme uses a proximity sensor on the casing to determine a time blade arrival time. From the blade arrival time one can estimate the blade deflection. The blade deflection will reflect the superposition of all the aeromechanical modes. However, due to their separation in frequency, the modal content can easily be decomposed.

The actuation approach is to place volumetric sources aft of the blade-row to modulate the back pressure and mass flow as a function of angular position and time resulting in unsteady loading of the blades. This in turn modifies the blade lift, generating the desired commanded force on the blades. By arranging an array of such actuators around the circumference one can create a pattern of forces on the blades. These patterns can form traveling waves that have the spatial shape of the aeromechanical modes. The experimental implementation of active flutter control on a fan rig presented in this paper consisted of an array of audio speaker-powered volumetric sources connected to the flow path equally spaced along the circumference axially located between the fan rotor blades and its exit stator guide vanes.

In experiments on a fan rig a linear observer was implemented to estimate the aeromechanical modal content of the blade row. This approach required a linear model for the dynamics of interest. Such a model was obtained for each aeromechanical mode by running swept-sine experiments in the system and measuring the complex ratio between the modal forcing function and the blade deflection at a point in the fixed frame. Then a low order (typically second order) state-space linear system was fit to the frequency response data. The observer was designed based on the aggregate of all these state-space blocks. An observer-based pole-placing technique was used to design a linear control law to add the desired amount of damping to flutter modes. The control system was able to add damping to three flutter modes. The damping augmentation achieved was an order of magnitude larger than the intrinsic aeromechanical damping of the flutter modes on the most stable operating condition of the fan.

Experiments described in this section were conducted under internal funding. Modeling and analysis were partially funded under previous AFOSR grants. The publications Banaszuk *et al.*, IFAC 2002, CDC 2002, AIAA 2003 of the results were funded under current AFOSR grant.

2.5.1 Notation

N - number of blades.
n - index of a flutter mode, $n = \ldots, -2, -1, 0, 1, 2, \ldots$.
$-\zeta_n$ - real part of the n-th flutter mode pole.
ω_{nr} - imaginary part of the n-th flutter mode pole, circular (pseudo) frequency of the n-th flutter mode in the rotating frame.
ω_{ns} - imaginary part of the n-th flutter mode pole, circular frequency of the n-th flutter mode in the stationary frame.
ξ_n - damping coefficient of the n-th flutter mode, $\xi_n := \frac{\zeta_n}{\sqrt{\zeta_n^2+\omega_{ns}^2}}$.
δ_n - Logarithmic decrement of the n-th flutter mode, $\delta_n := 2\pi\frac{\zeta_n}{\omega_{ns}} = 2\pi\frac{\xi_n}{\sqrt{1-\xi_n^2}}$.
θ_r - angle in the rotating frame.
θ_s - angle in the stationary frame.
$\alpha_{nr}(t, \theta_r)$ - blade deflection angle at time t at angle θ_r (in the rotating frame).
$\alpha_{ns}(t, \theta_s)$ - blade deflection angle at time t at angle θ_s (in the stationary frame).
ω_r - circular rotor frequency.
θ_{s0} - angle between the fixed reference points on the rotor and the stator at time $t = 0$.
$(\cdot)_n$ - n-th spacial Fourier coefficient.
$(\hat{\cdot})$ - temporal Fourier transform.

2.5.2 Flutter models

For an integer n (positive, zero, or negative) we model the n-th flutter mode, or n-th nodal diameter flutter mode, as a travelling wave in which all blades are oscillating harmonically with a constant phase angle $\theta_n := \frac{2\pi n}{N}$ relative to each other [18].

Let θ_r denote the angle measured relative to a fixed point on the rotor in the direction of the rotation. Assume that we have continuum of blades and there is no external forcing. We postulate that the n-th nodal component of the blade deflection at angle θ_r at time t is given by the formula

$$\alpha_{nr}(t, \theta_r) = A_n e^{-\zeta_n t}\cos(\omega_{nr}t - n\theta_r + \phi_{nr}) \tag{2.42}$$

where $-\zeta_n$ and ω_{nr} are, respectively, the real and imaginary part of the n-th flutter mode pole. Note that ω_{nr} is also the (pseudo) frequency of the n-th flutter mode in the rotating frame, and A_n and ϕ_{nr} are the initial magnitude and phase angle of the n-th flutter mode. The damping of the n-th flutter mode is usually described by one of two coefficients: the *damping coefficient* $\xi_n := \frac{\zeta_n}{\sqrt{\zeta_n^2+\omega_{ns}^2}}$ or the *logarithmic decrement* $\delta_n := 2\pi\frac{\zeta_n}{\omega_{ns}} = 2\pi\frac{\xi_n}{\sqrt{1-\xi_n^2}}$. Note that:

(1) The m-th blade is moving according to equation (2.42) with the corresponding angle $\theta_r = \frac{2\pi m}{N} + \theta_1$, where θ_1 is the position of the first blade relative to the fixed reference point on the rotor, $m = 1, 2, \ldots, N$.

(2) For a fixed time t and $n \neq 0$ the blade deflection $\alpha_{nr}(t, \theta_r)$ considered as a function of the angle θ_r has a sinusoidal shape with $|n|$ nodes. For $n = 0$ and a fixed time t the deflection is the same for each blade.

(3) For $\zeta_n = 0$ and $n \neq 0$ the blade deflection $\alpha_{nr}(t, \theta_r)$ is a wave with a fixed sinusoidal shape travelling around the annulus. The speed and the direction of rotation can be obtained by considering movement in time of the angle corresponding to one of the peaks of the wave. For instance, the first peak is obtained by solving the equation $\omega_{nr}t - n\theta_r + \phi_{nr} = \frac{\pi}{2}$ for θ_r. We have

$$\theta_r = \frac{1}{n}(\omega_{nr}t + \phi_{nr} - \frac{\pi}{2}). \tag{2.43}$$

Therefore, the speed of the wave is $\frac{\omega_{nr}}{|n|}$ and the direction is positive (the same as the direction of rotation of the rotor) for $n > 0$ and negative (the opposite to the rotor's rotation direction) for $n < 0$. We call the flutter modes travelling in the same direction as the rotor the *forward* travelling modes and the ones travelling in the direction opposite to the rotor's direction the *backward* travelling modes. (4) For a fixed angle θ_r, the blade deflection $\alpha_{nr}(t, \theta_r)$ considered as a function of time represents a response of a damped oscillator, i.e., a second order system with poles $-\zeta_n + i\omega_{nr}$ and $-\zeta_n - i\omega_{nr}$. Note that each particular blade oscillates with frequency ω_{nr}, which is n times bigger than the frequency of the corresponding travelling wave.

Now we express the motion of a blade due to a particular flutter mode as measured at an arbitrary angle on the stator.

Let ω_r denote the circular rotor frequency. Fix a reference point on the stator. The angles in the stationary frame will be measured relative to this point with positive direction corresponding to the rotor's rotation direction. Let θ_{s0} denote the angle at which the reference point on the stator is seen from the reference point on the rotor at time $t = 0$. Then, for an arbitrary time t, a fixed angle θ_s on the stator is related to the corresponding point on the rotor θ_r (measured in the rotating frame) by the formula $\theta_r = \theta_s + \theta_{s0} - \omega_r t$. Therefore, the deflection of the blade passing a fixed angle θ_s on the stator at time t is given by the formula

$$\begin{aligned} &\alpha_{ns}(t, \theta_s) = \alpha_{nr}(t, \theta_s + \theta_{s0} - \omega_r t) = \\ &A_n e^{-\zeta_n t} \cos((\omega_{nr} + n\omega_r)t - n\theta_s + \phi_{ns}) \end{aligned} \tag{2.44}$$

where $\phi_{ns} := \phi_{nr} - n\theta_{s0}$ is the initial phase of the n-th mode in the stationary frame.

Note that for $\zeta_n = 0$ and $n \neq 0$ the blade deflection $\alpha_{ns}(t, \theta_s)$ in the stationary frame is a wave with a fixed sinusoidal shape travelling around the rotor. In particular, a single blade vibration frequency in the stationary frame is $\omega_{ns} := \omega_{nr} + n\omega_r$.

The velocity of the rotation of the wave can be obtained in a similar manner as in the rotating frame case. In particular, the velocity of the wave corresponding n-th flutter mode in the stationary frame is $\omega_r + \frac{\omega_{nr}}{n}$. Let us recall that the latter is the velocity at which a fixed point on the graph of the blade deflection as a function of angle (say, a peak) is travelling around the annulus at the stationary frame. This velocity should not be confused with an individual blade velocity due to n-th flutter modes, i.e., ω_{ns}, which is n times bigger.

In the sequel we are going to use the stationary frame only. Therefore, we will often skip the subscript s and use θ to denote the angles measured in the stationary frame.

Since at a fixed time the flutter modes and the corresponding forcing functions have a fixed sinusoidal shape, they can be represented via their *spatial Fourier coefficients* (SFCs). One complex Fourier coefficient can be used to describe a single sinusoidal travelling wave. A general travelling wave with n-th nodal spatial shape and a temporal frequency ω_0 has the form $f_n(t,\theta) := F_n(t)\cos(\omega_0 t - n\theta + \phi) = F_n(t)\cos(\omega_0 t + \phi)\cos(n\theta) + F_n(t)\sin(\omega_0 t + \phi)\sin(n\theta)$. The corresponding SFC is, for $n \neq 0$, equal to $\widetilde{f}_n(t) := \frac{1}{\pi}\int_0^{2\pi} f_n(t,\theta)e^{jn\theta}d\theta$. One has $\widetilde{f}_n(t) = \frac{1}{\pi}\int_0^{2\pi} F_n(t)\frac{1}{2}(e^{j(\omega_0 t - n\theta + \phi)} + e^{-j(\omega_0 t - n\theta + \phi)})e^{jn\theta}d\theta = \frac{1}{2\pi}F_n(t)\int_0^{2\pi}(e^{j(\omega_0 t + \phi)} + e^{-j(\omega_0 t - 2n\theta + \phi)})d\theta$
$= F_n(t)(\cos(\omega_0 t + \phi) + j\sin(\omega_0 t + \phi))$. For $n = 0$, one has $\widetilde{f}_0(t) := \frac{1}{2\pi}\int_0^{2\pi} f_0(t,\theta)d\theta$. Thus, $\widetilde{f}_0(t) = \frac{1}{2\pi}\int_0^{2\pi} F_0(t)\cos(\omega_0 t + \phi)d\theta = F_0(t)\cos(\omega_0 t + \phi) = f_0(t,\theta)$, for all θ.

To reconstruct a wave from its SFC one can use the inverse spatial Fourier tranform

$$f_n(t,\theta) = Re(\widetilde{f}_n(t)^* e^{jn\theta}) = Re(\widetilde{f}_n(t)e^{-jn\theta}), \tag{2.45}$$

where $(\cdot)^*$ stands for the complex conjugation.

Observe that for $n \neq 0$:

(1) The magnitude and phase of the complex number representing the spatial Fourier coefficient of the wave $f_n(t,\theta)$ are the same as magnitude and phase of the wave.

(2) The real and imaginary part of the spatial Fourier coefficient of the wave $f_n(t,\theta)$ are the *Fourier series coefficients* of $f_n(t,\theta)$, i.e., the coefficients of $f_n(t,\theta)$ represented as a linear combination of $\cos(n\theta)$ and $\sin(n\theta)$, respectively.

Assume that the magnitude and phase of the wave $f_n(t,\theta)$ are constant in time with $F_n(t) := F_n$, for some $n \neq 0$. Then $f_n(t,\theta)$, and hence $\tilde{f}_n(t)$, is a periodic function of t and one can define the *temporal Fourier transform* of the spatial Fourier coefficient of the wave $f_n(t,\theta)$ $\hat{\tilde{f}}_n(j\omega) := \int_{-\infty}^{\infty} \tilde{f}_n(t)e^{-j\omega t}dt := \int_{-\infty}^{\infty} F_n(t)e^{j(\omega_0 t+\phi)}e^{-j\omega t}dt := F_n(t)e^{j\phi}\delta(\omega-\omega_0)$, where $\delta(\cdot)$ stands for the delta operator. Thus, the travelling waves with the temporal frequency ω_0 can be recognized in the (temporal) frequency domain as "spikes" at one single frequency ω_0. Spikes at positive frequencies represent the forward travelling waves, whereas the spikes at negative frequencies represent the backward travelling waves.

The case $n = 0$ is different. As we have noticed before, the spatial Fourier coefficient $\tilde{f}_0(t)$ of the function $f_0(t,\theta)$ coincides with the function $f_0(t,\theta)$ itself. Its temporal Fourier transform is $\hat{\tilde{f}}_0(j\omega) := \int_{-\infty}^{\infty} \tilde{f}_0(t)e^{-j\omega t}dt = \int_{-\infty}^{\infty} F_0(t)\frac{1}{2}(e^{j(\omega_0 t+\phi)} + e^{-j(\omega_0 t+\phi)})e^{-j\omega t}dt$
$= \frac{F_n(t)}{2}(e^{j\phi}\delta(\omega-\omega_0)+e^{-j\phi}\delta(\omega+\omega_0))$. One observes that the temporal Fourier transform of the spatial Fourier coefficient of the function $f_0(t,\theta)$ has two "spikes": one at ω_0 and the other at $-\omega_0$.

While the flutter modes for $n \neq 0$ are represented by travelling waves, they can be excited by forcing inputs that are either travelling waves of the form $f_n(t,\theta) := F_n\cos(\omega_0 t - n\theta + \phi)$ or by the *standing waves* of the form

$$f_n(t,\theta) := F_n\cos(\omega_0 t + \phi)\cos(n\theta). \tag{2.46}$$

This is due to the fact that a standing wave can be represented as linear combination of two travelling waves: $F_n\cos(\omega_0 t+\phi)\cos(n\theta) = \frac{1}{2}F_n(\cos(\omega_0 t - n\theta + \phi) + \cos(\omega_0 t + n\theta + \phi))$.

The temporal Fourier transform of the standing wave (2.46) is $\hat{\tilde{f}}_n(j\omega) := \int_{-\infty}^{\infty} \tilde{f}_n(t)e^{-j\omega t}dt = \int_{-\infty}^{\infty} F_n(t)\frac{1}{2}(e^{j(\omega_n t+\phi)} + e^{-j(\omega_n t+\phi)})e^{-j\omega t}dt$
$= \frac{F_n(t)}{2}(e^{j\phi}\delta(\omega-\omega_n)+e^{-j\phi}\delta(\omega+\omega_n))$. Note that the latter formula is valid for all integers n, including $n = 0$.

2.5.3 Flutter models with control

We assume that we have continuum of actuators around the stator that influence flutter modes. We will control the n-th flutter mode with a control function $u(t,\theta)$ that, as a function of angle, has the same shape as the n-th flutter mode wave. The control magnitude and phase will be chosen appropriately as functions of the measured (or reconstructed using an observer) magnitude and phase of the n-th flutter mode. the angle in the stationary frame, previously denoted by θ_s.) Similarly, for the identification purposes, one can force the n-th flutter mode with a using a wave of the with a constant magnitude and phase. More precisely, assume that the control input forcing function for the n-th mode is a *travelling wave* having some temporal frequency ω_0 and having the same shape as the n-th flutter mode:

$$\begin{aligned} u_n(t,\theta) = U_n\cos(\omega_0 t + \phi_{nu} - n\theta) = \\ U_n\cos(\omega_0 t + \phi_{nu})\cos(n\theta) + \\ U_n\sin(\omega_0 t + \phi_{nu})\sin(n\theta), \end{aligned} \tag{2.47}$$

for some constant U_n and ϕ_{nu}. The SFC of this forcing function is $\tilde{u}_n(t) = U_n e^{j(\omega_0 t+\phi_{nu})}$. The corresponding temporal Fourier transform is $\hat{\tilde{u}}_n(j\omega) = U_n e^{j\phi_{nu}}\delta(\omega-\omega_0)$.

We also assume that the steady-state n-th flutter mode component of the blade deflection response to the n-th nodal forcing of the form (2.47) is a travelling wave with the same spatial shape and temporal frequency, possibly shifted in phase by some angle ϕ_n relative to the forcing function:

$$\begin{aligned} &\alpha_n(t,\theta) = A_n\cos(\omega_0 t - n\theta + \phi_n) = \\ &A_n\cos(\omega_0 t + \phi_n)\cos(n\theta) + \\ &A_n\sin(\omega_0 t + \phi_n)\sin(n\theta) \end{aligned} \tag{2.48}$$

for some constant A_n and ϕ_n that, for fixed U_n and ϕ_{nu}, are functions of ω_0.

The SFC of the n-th component of the blade deflection is $\tilde{\alpha}_n(t) = A_n e^{j(\omega_0 t + \phi_n)}$. The temporal Fourier transform of the SFC of the n-th component of the blade deflection is $\hat{\tilde{\alpha}}_n(j\omega) = A_n e^{j\phi_n}\delta(\omega - \omega_0)$. We assume that we measure the blade displacement at finite number of locations on the stator. (This is going to be accomplished with eddy current sensors.) At a fixed angle θ_y the measured blade dispalcement is going to be

$$\begin{aligned} &y_{n\theta_y}(t) := \alpha_n(t,\theta_y) = \\ &A_n\cos(\omega_0 t - n\theta_y + \phi_n) \\ &= A_n\cos(\omega_0 t + \phi_n)\cos(n\theta_y) + \\ &A_n\sin(\omega_0 t + \phi_n)\sin(n\theta_y). \end{aligned} \tag{2.49}$$

The temporal Fourier transform of the output function is $\hat{y}_n(j\omega) = \frac{A_n}{2}(e^{j(\phi_n - n\theta_y)}\delta(\omega - \omega_0) + e^{-j(\phi_n - n\theta_y)}\delta(\omega + \omega_0))$.

Now we present dynamic system models for the evolution of the n-th flutter mode subject to control. The description adapts an approach to model rotating stall from [42].

One can obtain a low order model describing the dynamics of the n-th flutter suitable for control purposes in the following three steps.

1. Conduct an experiment to obtain the transfer function between the n-th SFC of the forcing function given by (2.47) and the corresponding n-th SFC of the blade deflection function given by (2.48).
2. Fit a low-order transfer function to the one obtained experimentally.
3. Obtain a state-space realization of the low-order transfer function obtained in step 2.

We assume that the uncontrolled n-th flutter mode behaves like a lightly damped harmonic oscillator with individual blades moving in the stationary frame according to the formula (2.44). Thus, we expect the mode to have a significant response to forcing only at a narrow band of frequencies of interest around the mode's natural frequency $\omega_{ns} := \omega_{nr} + n\omega_r$. The control goal is to add damping to the mode by a feedback control only at this narrow band of frequencies. Therefore, it is sufficient to have an approximate low order model describing the dynamics of the n-th mode at this narrow frequency range. Even if the frequency response of the n-th flutter mode were that of a low pass, rather than a band pass filter and the actuator dynamics cannot be neglected over a wide band of frequencies, so that a narrow band frequency model will not be accurate at low frequencies, the inaccuracy of the model will not significantly impact control performance. The controllers will have a band pass characteristic, so that the unmodelled dynamics at both low and high frequencies will not be destabilized.

The transfer function between the n-th SFC's of the forcing function and the corresponding blade deflection response is defined by

$$G_n(j\omega) := \frac{\hat{\tilde{\alpha}}_n(j\omega)}{\hat{\tilde{u}}_n(j\omega)} = \frac{A_n}{U_n}e^{j(\phi_n - \phi_{nu})}. \tag{2.50}$$

Both A_n and ϕ_n are, in general, functions of the frequency ω.

To obtain the transfer function $G_n(j\omega)$ from a sine sweep experiment, one has to access the function $\tilde{\alpha}_n(t)$. To obtain an approximation to $\tilde{\alpha}_n(t)$ one would have to simultaneously measure the blade displacement $\alpha_n(t,\theta)$ at some finite number of angles around the annulus and use a discrete approximation of the integral defining the spatial Fourier transform. A reasonable approximation would require at least $2n+1$ blade displacement sensors around the annulus.

However, even with one sensor one can measure the transfer function $G_n(j\omega)$ because of the following simple observation. Assume that we have a blade displacement sensor at some angle θ_y at the stationary frame. The measured output function $y_{n\theta_y}(t) := \alpha_n(t,\theta_y)$ is given by the equation 2.49. Assume also that we measure the value of the actuation function $u_n(t,\theta)$ at a fixed angle θ_u. Let $u_{n\theta_u}(t) := u_n(t,\theta_u)$. Note that $y_{n\theta_y}(t) = A_n\cos(\omega_0 t - n\theta_y + \phi_n)$ and $u_{n\theta_u}(t) = U_n\cos(\omega_0 t + \phi_{nu} - n\theta_u)$ have relative phase shift of $\phi_n - \phi_{nu} - n(\theta_y - \theta_u)$. Hence, the measured transfer function between them during a sine sweep experiment is $G_{n\theta_u\theta_y}(j\omega) := \frac{\hat{y}_{n\theta_y}(j\omega)}{\hat{u}_{n\theta_u}(j\omega)} = \frac{A_n}{U_n}e^{j(\phi_n-\phi_{nu}-n(\theta_y-\theta_u))} = e^{-jn(\theta_y-\theta_u)}G_n(j\omega)$. Therefore, $G_n(j\omega)$ can be obtained from $G_n(j\omega) = e^{jn(\theta_y-\theta_u)}G_{n\theta_u\theta_y}(j\omega)$.

One can observe that, except for the case $n = 0$, any description of transfer functions $G_n(j\omega)$ as a rational function of $j\omega$ valid in a wide frequency band must have *complex* rather than real coefficients. To see that, note that a transfer function $G(j\omega)$ with real coefficients has the property $G(-j\omega) = G(j\omega)^*$, i.e., it has a Nyquist diagram symmeric with respect to the real axis. We know from experiments that the response of the n-th flutter mode to the forward or backward travelling forcing wave with the same temporal frequency is not symmetric. Thus, for $n \neq 0$, one has $G_n(-j\omega) \neq G_n(j\omega)^*$. However, we do expect the reponse to be symmetric for $n = 0$, so that we have $G_0(j\omega) = G_0(-j\omega)^*$. Therefore, we expect the transfer function $G_0(j\omega)$ considered as a rational function of $j\omega$ to have real coefficients. Because of this difference between the cases $n \neq 0$ and $n = 0$, we are going to derive the corresponding models separately.

A low order, narrow band model for the transfer function $G_n(j\omega)$ between the n-th SFC of the forcing function given by (2.47) and the corresponding output function given by (2.49) for $n \neq 0$ is a *first order* transfer function with *complex* coefficients

$$G_n(j\omega) = \frac{b_{nR} + jb_{nI}}{\zeta_n + j(\omega - \omega_{ns})}. \tag{2.51}$$

A complex-valued state-space realization of this transfer function is

$$\dot{\tilde{\alpha}}_n(t) = (-\zeta_n + j\omega_{ns})\tilde{\alpha}_n(t) + (b_{nR} + jb_{nI})\tilde{u}_n(t). \tag{2.52}$$

Note that both $\tilde{\alpha}_n(t)$ and $\tilde{u}_n(t)$ are *complex* valued functions of time. Observe also that the unforced response of (2.52) is $\tilde{\alpha}_n(t) = e^{(-\zeta_n + j\omega_{ns})t}\tilde{\alpha}_n(0)$, which agrees with postulated unforced evolution of the n-th flutter mode given by (2.44).

Let us emphasize again that the simple transfer function model (2.51) and its state-space realization (2.52) are valid only for a narrow range of frequencies around the flutter frequency ω_{ns}. The actuator characteristic over that frequency range is simply represented by the magnitude and phase of the n-th mode of the actuator disk at the flutter frequency and incorporated into the complex number $b_{nR} + jb_{nI}$. This approximation is reasonable, as long as the actuator frequency response does not change significantly over the frequency interval of interest and a feedback controller characteristic will be that of a sufficiently narrow band-pass filter. If this is not the case, the actuator dynamics should be incorporated in the model.

An equivalent description to (2.51) is possible with a real-valued model of real dimension two. In the sequel the subscripts $(\cdot)_R$ and $(\cdot)_I$ will denote the real and imaginary part of a complex number. One can easily check [42] that the real and imaginary part of the SFC's of blade displacement and forcing function satisfy the following set of two differential equations

$$\begin{aligned} \begin{bmatrix} \dot{\tilde{\alpha}}_{nR}(t) \\ \dot{\tilde{\alpha}}_{nI}(t) \end{bmatrix} = \begin{bmatrix} -\zeta_n & -\omega_{ns} \\ \omega_{ns} & -\zeta_n \end{bmatrix} \begin{bmatrix} \tilde{\alpha}_{nR}(t) \\ \tilde{\alpha}_{nI}(t) \end{bmatrix} + \\ \begin{bmatrix} b_{nR} & -b_{nI} \\ b_{nI} & b_{nR} \end{bmatrix} \begin{bmatrix} \tilde{u}_{nR}(t) \\ \tilde{u}_{nI}(t) \end{bmatrix}. \end{aligned} \tag{2.53}$$

The corresponding transfer function desription is

$$\begin{bmatrix} \hat{\tilde{\alpha}}_{nR}(j\omega) \\ \hat{\tilde{\alpha}}_{nI}(j\omega) \end{bmatrix} = \begin{bmatrix} G_{nr}(j\omega) & -G_{ni}(j\omega) \\ G_{ni}(j\omega) & G_{nr}(j\omega) \end{bmatrix} \begin{bmatrix} \hat{\tilde{u}}_{nR}(j\omega) \\ \hat{\tilde{u}}_{nI}(j\omega) \end{bmatrix}. \tag{2.54}$$

One can verify that

$$G_{nr}(j\omega) = \frac{b_{nR}(j\omega + \zeta_n) - b_{nI}\omega_{ns}}{(j\omega + \zeta_n)^2 + \omega_{ns}^2} \tag{2.55}$$

$$G_{ni}(j\omega) = \frac{-b_{nI}(j\omega + \zeta_n) - b_{nR}\omega_{ns}}{(j\omega + \zeta_n)^2 + \omega_{ns}^2} \tag{2.56}$$

and

$$G_n(j\omega) = G_{nr}(j\omega) + jG_{ni}(j\omega). \tag{2.57}$$

Assume that a blade displacement sensor is located at some angle θ at the stationary frame. The measured output function $y_{n\theta}(t) := \alpha_n(t, \theta)$ can be expressed in terms of the real and imaginary parts of the SFC of $\alpha_n(t, \theta)$ via the inverse spatial Fourier transform (2.45) as $y_{n\theta}(t) = Re(\tilde{\alpha}_n(t)e^{-jn\theta}) = Re(\tilde{\alpha}_{nR}(t) + j\tilde{\alpha}_{nI}(t))(\cos(n\theta) - j\sin(n\theta)) = \cos(n\theta)\tilde{\alpha}_{nR}(t) + \sin(n\theta)\tilde{\alpha}_{nI}(t)$. Let

$$x_n(t) := \begin{bmatrix} \tilde{\alpha}_{nR}(t) \\ \tilde{\alpha}_{nI}(t) \end{bmatrix}, v_n(t) := \begin{bmatrix} \tilde{u}_{nR}(t) \\ \tilde{u}_{nI}(t) \end{bmatrix}, \tag{2.58}$$

$$\begin{aligned} A_n &:= \begin{bmatrix} -\zeta_n & -\omega_{ns} \\ \omega_{ns} & -\zeta_n \end{bmatrix}, B_n := \begin{bmatrix} b_{nR} & -b_{nI} \\ b_{nI} & b_{nR} \end{bmatrix}, \\ C_{n\theta} &:= [\cos(n\theta) \sin(n\theta)]. \end{aligned} \tag{2.59}$$

The state and the output equation for the n-th nodal flutter mode can be concisely written as

$$\begin{aligned} \dot{x}_n(t) &= A_n x_n(t) + B_n v_n(t) \\ y_{n\theta}(t) &= C_{n\theta} x_n(t). \end{aligned} \tag{2.60}$$

If there is only one sensor at some fixed angle θ, we will skip the subscript θ in the description of $y_{n\theta}(t)$ and $C_{n\theta}$.

Observe that all the quantities in the equation (2.60) are real. One can identify the parameters in the model using travelling wave excitation, as described in the previous section. Alternatively, one can exploit the skew-symmetric structure of the matrices A_n and B_n and use only one of the inputs of $v_n(t)$ for excitation. This amounts to forcing the system with a standing wave, rather than travelling wave pattern.

Now we propose a real-valued model for control of the 0-th nodal flutter of dimension two. Assume that a blade displacement sensor is located at some angle θ at the stationary frame. The measured output function is $y_{0\theta}(t) := \alpha_0(t, \theta) = \tilde{\alpha}_0(t)$. Let

$$G_0(j\omega) := \frac{\hat{\tilde{\alpha}}_0(j\omega)}{\hat{\tilde{u}}_0(j\omega)} = \frac{\hat{\alpha}_0(j\omega)}{\hat{u}_0(j\omega)} = \frac{A_0}{U_0} e^{j(\phi_0 - \phi_{0u})}. \tag{2.61}$$

A simplest model for $G_0(j\omega)$ with real coeffcients that exhibits a behavior of a lightly damped oscillator is

$$G_0(j\omega) = \frac{b_1(j\omega) + b_0}{(j\omega + \zeta_0)^2 + \omega_0^2}, \tag{2.62}$$

for some real b_1, b_0, ζ_0, and ω_0. The corresponding state-space description (in the observer canonical form) is

$$\begin{aligned} \dot{x}_0(t) &= A_0 x_0(t) + B_0 v_0(t) \\ y_{0\theta}(t) &= C_{0\theta} x_0(t), \end{aligned} \tag{2.63}$$

where

$$v_0(t) := u_0(t), \tag{2.64}$$

$$A_0 := \begin{bmatrix} -\zeta_0 & 1 \\ -\omega_0^2 & 0 \end{bmatrix}, B_0 := \begin{bmatrix} b_1 \\ b_0 \end{bmatrix}, C_{0\theta} := [1\ 0]. \tag{2.65}$$

Let consider a finite number k_f of flutter modes with nodal numbers n_1, n_2, ..., n_{k_f}. Assume that as the measurement outputs we use m blade displacement sensors located at the angles θ_1, θ_2, ..., θ_m, respectively. We assume that the blade displacement y_θ measured at some angle θ at the stationary frame is the sum of the diplacements due to particular flutter modes:

$$y_\theta(t) = \textstyle\sum_{k=1}^{k_f} \alpha_{n_k}(t, \theta). \tag{2.66}$$

We can write down the following state-space model describing the dynamics of the k_f most active flutter modes:

$$\begin{aligned} \dot{x}(t) &= Ax(t) + Bv(t) \\ y(t) &= Cx(t), \end{aligned} \tag{2.67}$$

where $x(t) := [x_{n_1}(t) \dots x_{n_{k_f}}(t)]^T$,
$v(t) := [u_{n_1}(t) \dots u_{n_{k_f}}(t)]^T$, $y(t) := [y_{\theta_1}(t) \dots y_{\theta_m}(t)]^T$, A and B are block diagonal matrices containing A_{n_j} and B_{n_j} blocks, respectively, and C is a matrix composed of $C_{n\theta}$ blocks.

The dimension of the output variable $y(t)$ is equal to m, which is the number of blade displacement sensors (e.g., eddy current sensors) used for measurement.

One may be tempted to place many sensors to make the C matrix invertible and use a full-state static feedback to arbitrarily place the damping of the flutter modes. This strategy might be succesfull for flutter modes with the nodal number $n_k \neq 0$ if the variations of the actuator dynamics with frequency can be neglected. However, note that C is never invertible if one includes the 0-th nodal flutter dynamics, as $C_{0\theta} = [1\ 0]$ for all θ, and hence C has a column of zeros. Moreover, a strong output noise component, which includes all unmodelled sources of blade displacement, such as periodic forcing due to rotor and blades assymetry, neglected flutter modes, rotating stall dynamics, an inlet distorsion, etc., would make reconstructing the state of the flutter modes by inverting the C matrix problematic.

To circumvent the problems with direct inversion of the C matrix and the output noise, and at the same time reduce the number of blade displacement sensors, we are going to reconstruct the state of the system using an observer. As we will see, in principle, just one blade displacement sensor is sufficient for this purpose.

2.5.4 Model of the disturbances

We are going to augment the state-space model (2.67) by adding some noise sources in the state and output equations. We assume that the system is described by the equation

$$\begin{aligned} \dot{x}(t) &= Ax(t) + Bv(t) + e_x(t) \\ y(t) &= Cx(t) + e_y(t), \end{aligned} \tag{2.68}$$

where $e_x(t)$ is an unknown disturbance driving the state of the system, and $e_y(t)$ is an unknown output disturbance. We assume that the state disturbance $e_x(t)$ has a strong periodic component with the rotor frequency due to rotor and blades assymetry and some random fluctuations due to inlet distorsion that excite the k_f flutter modes of interest. The output disturbance $e_y(t)$ might include all unmodelled sources of blade displacement such as neglected flutter modes, rotating stall dynamics, a strong constant component (so-called DC-component) due to sensor bias and rotor assymetry, a periodic component due to differences between particular blades, $60Hz$ electric noise and its harmonics from electric components and possibly some other measurement noise.

We expect the constant and periodic components of the disturbances to be dominant. We are going to extend our model to incorporate these components and reconstruct them using an observer. We assume that the actual blade displacement $y_{a\theta}(t)$ measured by a sensor located at an angle θ on the stator is given by $y_{a\theta}(t) = y_\theta(t) + y_{dc}(\theta) + y_p(\omega_r t - \theta) + y_{wn}(t, \theta)$, where $y_\theta(t)$ is the sum of the blade displacement components due to the dynamics of the selected most active k_f flutter modes of interests given by (2.66), $y_{dc}(\theta)$ is an unknown constant bias component, $y_p(\omega_r t - \theta)$ represents a steady unknown periodic motion, and $y_{un}(t, \theta)$ is the broad band component of the measured output.

Note that the forcing of the blades due to rotor and casing assymetry will cause a different constant blade diplacement at a different angular location at the stationary frame, even the the magnitude of the angular motion of the blades is the same. Also, a constant bias signal may be different fo each sensor. Therefore, we do not expect to have the same constant component $\alpha_{dc}(\theta)$ at each output.

The unknown constant component of the k-th output $y_{\theta_k}(t)$ will be modelled as the state $x_{kdc}(t)$ of an integrator with an unknown initial condition added to the system (2.68) $\dot{x}_{kdc}(t) = A_{dc}x_{dc}(t)$, $y_{\theta_k}(t) = C_{dc}x_{kdc}(t)$, where $A_{dc} := [0]$, $C_{dc} := [1]$.

Particular blades on the rotor are slightly different. Moreover, the spacing between the blades may vary around the rotor. Thus, if the diplacement is measured by a difference of expected (assuming no blade motion due to flutter) and actual time of arrival of the blade (using eddy current or optical senors) and the time of expected arrival is calculated assuming a uniform spacing between the blades, a measurement of an angular blade displacement will have an error. In both cases mentioned above this error will have a form of a wave travelling forward with the speed equal to the rotor frequency ω_r. This justifies the choice of the form of the periodic disturbance $y_p(\omega_r t - \theta)$.

A constant component of $y_p(\omega_r t - \theta)$ can be incorporated into the constant disturbance $\alpha_{dc}(\theta)$. Therefore, without loss of generality one can assume that for each fixed t the average value of $y_p(\omega_r t - \theta)$ over θ is zero. For each $n > 0$ one can compute the spatial Fourier coefficient $\tilde{y}_{pn}(t)$ of $y_p(\omega_r t - \theta)$ and then represent the function $y_p(\omega_r t - \theta)$ using the inverse spatial Fourier transform (in other words, represent $y_p(\omega_r t - \theta)$ as Fourier series). After truncating the series at some $n = k_p$ one obtains the formula $y_p(\omega_r t - \theta) = \sum_{n=1}^{k_p} Re(\tilde{y}_{pn}(t)e^{-jn\theta}) = \sum_{n=1}^{k_p} \cos(n\theta)(a_n \cos(n\omega_r t) + b_n \sin(n\omega_r t))$ $+ \sin(n\theta)(a_n \sin(n\omega_r t) - b_n \cos(n\omega_r t))$, for some constants a_n, b_n, $n = 1, \ldots, k_p$. Observe that for fixed θ, the function $y_p(\omega_r t - \theta)$ can be treated as an output of a system of k_p uncoupled oscillators with frequencies equal to multiples of the rotor frequency ω_r. Therefore, the periodic disturbance $y_p(\omega_r t - \theta)$ will be modelled by adding states $x_{1e}(t), x_{2e}(t), \ldots, x_{k_p e}(t)$ of k_p oscillators to the system (2.68). Let $\omega_{ke} := k\omega_r$ and

$$A_{ke} := \begin{bmatrix} 0 & -\omega_{ke} \\ \omega_{ke} & 0 \end{bmatrix}, C_{n\theta} = [\cos(n\theta) \ \sin(n\theta)]. \tag{2.69}$$

We assume that the state of the oscillator $x_{ke}(t)$ satisfies the equation

$$\dot{x}_{ke}(t) = A_{ke}x_{ke}(t), \tag{2.70}$$

with an unknown initial condition. The function $y_p(\omega_r t - \theta)$ can be expressed as

$$y_p(\omega_r t - \theta) = \sum_{n=1}^{k_p} C_{n\theta}x_{ne}(t) \tag{2.71}$$

We assume that $y_{wn}(t, \theta)$, the unmodeled part of the output function, is a low level broad band noise.

We add the disturbance states $x_{1dc}(t), \ldots, x_{mdc}(t)$ and $x_{1e}(t), \ldots, x_{k_p e}(t)$ to the state $x(t)$ and form an augmented state variable $x_a(t)$. We can write down the following augmented state-space model describing the dynamics of the k_f most active flutter modes and the effect of disturbances on the output and state:

$$\begin{aligned} \dot{x}_a(t) &= A_a x_a(t) + B_a v(t) + e_{axu}(t) \\ y_a(t) &= C_a x_a(t) + e_{ayu}(t), \end{aligned} \tag{2.72}$$

where $e_{axu}(t)$ and $e_{ayu}(t)$ denote the broad-band components of the state and output disturbances (we skip the details of straightforward contruction of the augmented system matrices).

Note that the system (2.72) is not controllable, as we do not assume that we have any actuation authority over the part of the system that models the disturbances. Therefore, we can only attempt to place the eigenvalues of the system corresponding to the flutter modes. If the full state of (2.72) were available for measurement, we would use a feedback law of the form $v := -K_a x_a$, where K_a is of the form $K_a = [K\ 0]$ and K is chosen so that the eigenvalues of the matrix $A - BK$ are placed in the desired position. This can be achieved, as it follows from the Hautus criterion that the pair (A, B) is controllable since the flutter modes are separated in frequency. Note that the matrices A and B are block-diagonal. Hence, one can use a block diagonal feedback gain matrix K and separately place the eingenvalues of particular flutter modes. As we noticed, the state of the flutter modes is not directly available. However, one can use an observer state instead of the actual state for feedback.

2.5.5 Observer-based control of flutter

The main reason for incorporating the unknown disturbances into the state of the system is to reconstruct them along with the state of the flutter dynamics and filter out in this way the state of the flutter modes of interest. This state can be used for designing a full state feedback and achieve a prescribed level of damping of the flutter modes.

To verify if the augmented system (2.72) is observable one can use the Hautus criterion of observability [29]. The latter says that (2.72) if and only if the matrix

$$\begin{bmatrix} \lambda I - A_a \\ C_a \end{bmatrix} \tag{2.73}$$

has a full column rank $\forall \lambda \in \sigma(A_a)$, where $\sigma(\cdot)$ stands for the spectrum of a matrix. Note that the matrix A_a is block-diagonal. Thus, its spectrum is the collection of spectra of the matrices on the diagonal. One can easily see that as long as the flutter frequencies do not coincide with multiples of the rotor frequency, the system is observable even from a single sensor.

In the sequel we assume that the multiples of the rotor frequency are separated from the frequencies of the flutter modes, so that the pair (C_a, A_a) is observable.

An observer used to reconstruct flutter modes [29] has the form

$$\begin{aligned} \dot{\hat{x}}_a(t) &= A_a \hat{x}_a(t) + B_a v_a(t) + L(y_a(t) - \hat{y}_a(t)) \\ \hat{y}(t) &= C_a \hat{x}_a(t), \end{aligned} \tag{2.74}$$

with the observer gain matrix L chosen so that the observer error converges to zero. Let $\tilde{x}(t) := x_a(t) - \hat{x}_a(t)$ denote the error of observation. The error dynamics is given by

$$\dot{\tilde{x}}_a(t) = (A_a - LC_a)\tilde{x}_a(t) - Le_{ayu}(t) + e_{axu}(t). \tag{2.75}$$

To guarantee the convergence of the observer error to zero, the matrix L has been chosen such that the matrix $A_a - LC_a$ has all eigenvalues with negative real part. Since the pair (C_a, A_a) is observable, the eigenvalues of $A_a - LC_a$ can be assigned arbitrarily. By choosing the eigenvalues far enough from the imaginary axis one can make the observer error decaying arbitrarily fast. However, this requires high values of the entries of the observer gain matrix L. Since the unmodelled part of the measurement noise $e_{ayu}(t)$ affects the error dynamics (2.75) through the matrix L, a high gain observer is going to have a significant response to the measurement noise. Therefore, one has to choose the eigenvalues of the matrix $A_a - LC_a$ carefully, balancing the rate of the observer error decay with the sensitivity to output noise.

One can design a feedback controller for the system (2.72) in a form of a full-state feedback $v_a(t) = -K_a x_a(t)$, where $K_a = [K\ 0]$ is chosen so that the eigenvalues of the matrix $A - BK$ corresponding to the flutter modes have a prescribed level of damping [29]. Since the full state of (2.72) is not accessible for a direct measurement, one uses the state of the observer (2.74) in place of the state of (2.72) in the feedback law. i.e., $v_a(t) = -K_a \hat{x}_a(t)$. The state equations of the system consisting of an interconnection of the system (2.72) and the observer (2.74) are

$$\begin{aligned}\begin{bmatrix} \dot{x}_a(t) \\ \dot{\hat{x}}_a(t) \end{bmatrix} = \begin{bmatrix} A_a & -B_aK_a \\ LC_a & A_a - B_aK_a - LC_a \end{bmatrix} \begin{bmatrix} x_a(t) \\ \hat{x}_a(t) \end{bmatrix} + \\ \begin{bmatrix} I \\ 0 \end{bmatrix} e_{axu}(t) + \begin{bmatrix} 0 \\ L \end{bmatrix} e_{ayu}(t).\end{aligned} \tag{2.76}$$

The *Separation Principle* says that the set of eigenvalues of the overall system (2.76) is a union of the eigenvalues of the observer error matrix $A_a - LC_a$ and the eigenvalues of the matrix $A_a - B_aK_a$. In turn, the set of eigenvalues of $A_a - B_aK_a$ is the union of the eigenvalues of $A - BK$ and the eigenvalues of the modelled disturbance modes.

2.5.6 Flutter control experiments

Experiments with observer-based flutter control on 17″-fan test rig shown in Figure 2.13 . The rig has one fan stage with sixteen blades on a rotor powered with an external air turbine and one row of exit guide vanes on a stator. Variable fan exit area is controlled via translating throttle plug. By reducing the throttle area one increases the incidence angle of the air approaching the blades and thus reduces damping of stall flutter modes. The control system is shown in Figure 2.14. We used two or one eddy current sensors to measure the blade displacement in the stationary frame and ten speakers mounted in cavities located around the fan casing as actuators. All control experiments reported here done at

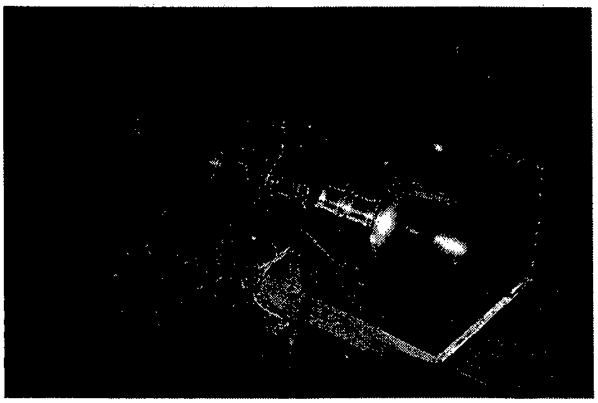

Figure 2.13: 17" fan experimental rig

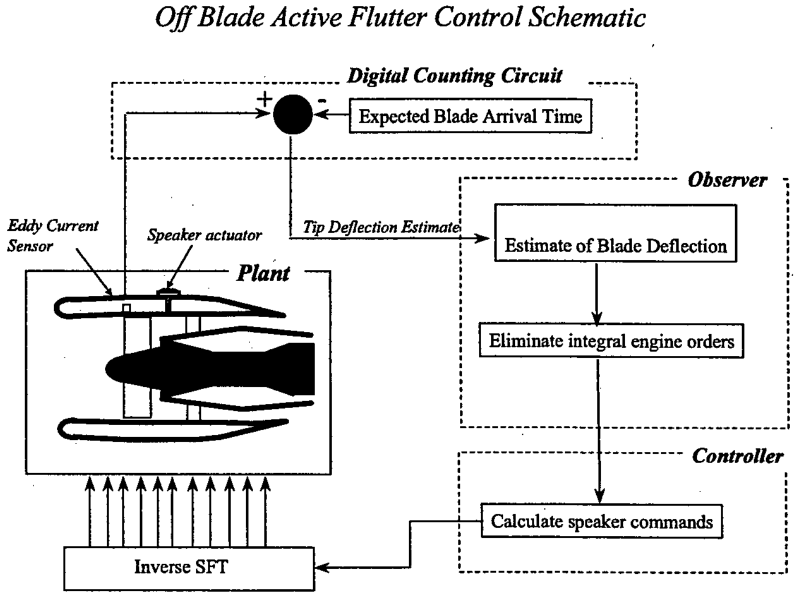

Figure 2.14: Flutter control system schematics

the rotor frequency 150 Hz (9000 RPM). Most expreriments were done at the most stable operating point at wide open throttle and some closer to flutter boundary.

The goal was to demonstrate that we can add significant amount of damping to the lightly damped flutter modes. The goal was achieved for the least stable fan flutter modes with nodal diameters 0, 1, and 2.

We identified the parameters of the real valued 2-nd order state-space models for the flutter modes 0, 1, and 2 from a sine sweep experiment. For nodal diameter 0 we assumed model given by equation (2.63). For the nodal diameters other than 0 we assumed model given by equation (2.60). We used a Matlab script that first fitted a 2-nd order transfer function (with two poles and one zero) to the experimentally obtained transfer fucntion from a spectral analyzer and then obtained an appropriate state-space realization. For nodal diameters $n = 1$ and $n = 2$ we used forcing with a standing wave cosine pattern, i.e., the input $\tilde{u}_{nR}(t)$. In this way we identified the matrices $C_{n\theta}$ (for two values of θ), A_n, and the first column of the matrix B_n. The matrix A_n was forced to be in the (modal) form (2.59). The second column of B_n was obtained from the first one.

Figures 2.15, 2.16 and 2.17 show the Bode plots from a sine-sweep experiment and the corresponding 2-nd order fits for flutter modes with nodal diameters $n = 0$, $n = 1$, and $n = 2$. The fits and models are obtained independently for each of the eddy current sensors (denoted $DT1$ and $DT2$, respectively).

Note that the 2-nd order transfer function fits to experimental data are good near the flutter frequency (i.e., the frequency at the resonant peak of the magnitude), but there is an increasing phase error away from the flutter frequency. Ass we will see, this phase mismatch represents unmodeled non-minumum phase dynamics that will somewhat limit performance of the control scheme based on the 2-nd order model.

Several observer-based schemes we tried in flutter control. Some of them used both sensors and

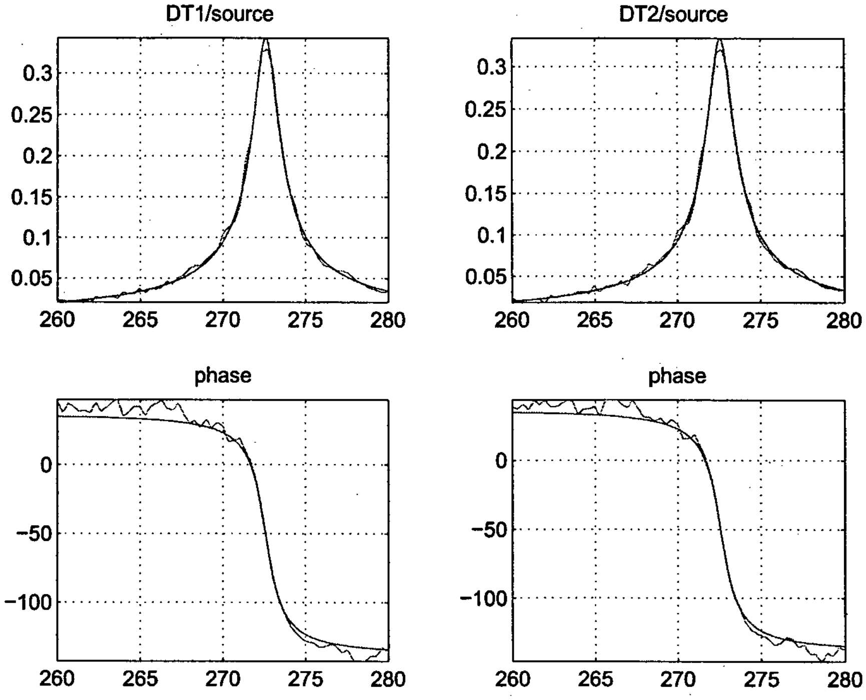

Figure 2.15: Bode plots for flutter mode $n = 0$. Experimental data and 2-nd order fits.

some of them used just one sensor. Number of flutter and disturbance modes also varied. All observers had a constant disturbance states (denoted dc) and from one to four pairs of the states modelling periodic disturbances at the multiples of the rotor frequency (denoted $1e$, $2e$, etc.). The available processor speed limited the number of observer states that could be used for control.

Each observer was designed in the form (2.74), with the gain matrix L chosen by specifying the damping of the observer poles. The specified observer damping was about twice the value of the desired damping of the flutter mode of interest, except for the dc states, which had much higher damping. The control law was a linear feedback from the observer state. Only the (estimated) flutter state was used for control. The feedback was designed to augment the damping of the flutter mode of interest to the desired level without changing its frequency.

The amount of damping added to particular flutter modes was obtained from a sine-sweep experiment. Bode plots for open and closed-loop systems were obtained. Since the 2-nd order transfer function fits were not acurate enough (see Figures 2.15, 2.16 and 2.17) to get a good estimate of damping, 4-th order transfer functions were fitted instead. The 4-th order fits were very good for 0-th and 1-st nodal diameter flutter modes, and reasonable for the 2-nd nodal diameter flutter mode.

The 0-th flutter mode was the least stable mode on 17-inch fan rig. At the most stable rig operating point the open-loop logarithmic decrement was $\delta_0 = 0.018$. The control scheme that achieved the biggest damping increase used only one DT sensor and was based on model with 7 states: 2-nd order models of the 0-th and 1-st flutter modes, 1-st order model of the dc bias of $DT1$ sensor, and a 2-nd order model of $2e$ signal. The closed-loop logarithmic decrement achieved was $\delta_0 = 0.21$.

Figure 2.18 shows open and closed-loop Bode plots for the plant and the 4-th order transfer function fits.

Figure 2.19 shows the spectral content of the time traces of one actuator, strain gauge on a blade, and $DT1$ (time difference between actual and expected blade arrival) signal. The frequency of the

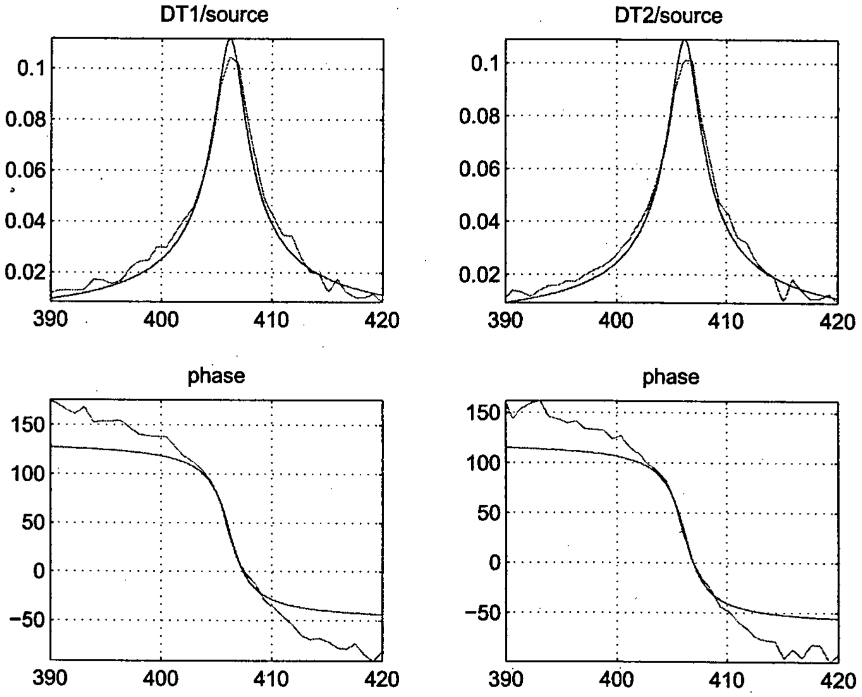

Figure 2.16: Bode plots for flutter mode $n = 1$. Experimental data and 2-nd order fits.

0-th flutter mode (about 273 Hz) is shown by a circle. The first three multiples of the rotor frequency (150 Hz) are marked by crosses. Note that the actuator has a strong component at the (unmodeled) $1e$ frequency, but no component at the (modeled) $2e$ frequency, even though there is a strong $2e$ signal in the $DT1$ signal. This illustrates the benefits of estimating the periodic disturbances at multiples of rotor frequency using an observer. Essentially, the periodic disturbance observer provides a notch filter in the transfer functions from blade arrival time difference to the speaker command. Adding more models of the periodic disturbances with muliples of the rotor frequency to the observer reduces the actuator energy waisted for response in that frequencies.

The 1-st flutter mode was the second least stable mode on 17-inch fan rig. At most stable rig operating point the open-loop logarithmic decrement was $\delta_1 = 0.028$. The control scheme that achieved the biggest damping increase used both $DT1$ and $DT2$ sensors and was based on model that had 8 states: 2-nd order models of 0-th and 1-st flutter modes, dc estimates for $DT1$ and $DT2$ sensors, and a 2-nd order model of $2e$ signal. The closed-loop logarithmic decrement was $\delta_1 = .153$. Figure 2.20 shows open and closed-loop Bode plots for the plant and the 4-th order transfer function fits.

The 2-nd flutter mode was the third least stable mode on 17-inch fan rig. At the most stable rig operating point the open-loop logarithmic decrement was $\delta_1 = 0.037$. We used both $DT1$ and $DT2$ sensors. The model used for observer design had 10 states: 2-nd order model of 2-nd flutter mode, dc estimates for $DT1$ and $DT2$ sensors, and 2-nd order models of $3e$, $4e$, and $5e$ disturbance signals. The closed-loop logarithmic decrement was $\delta_1 = .174$. Figure 2.21 shows open and closed-loop Bode plots for the plant and the 4-th order transfer function fits.

Figure 2.22 summarizes achieved damping augmentation.

We tested an observer-based controllers designed at the most stable operating point at the rotor frequency of 9000 RPM for the throttle position very close to the stability boundary of the $n = 0$ flutter mode. Figure 11 shows the open and closed-loop Bode plots and damping estimates. The

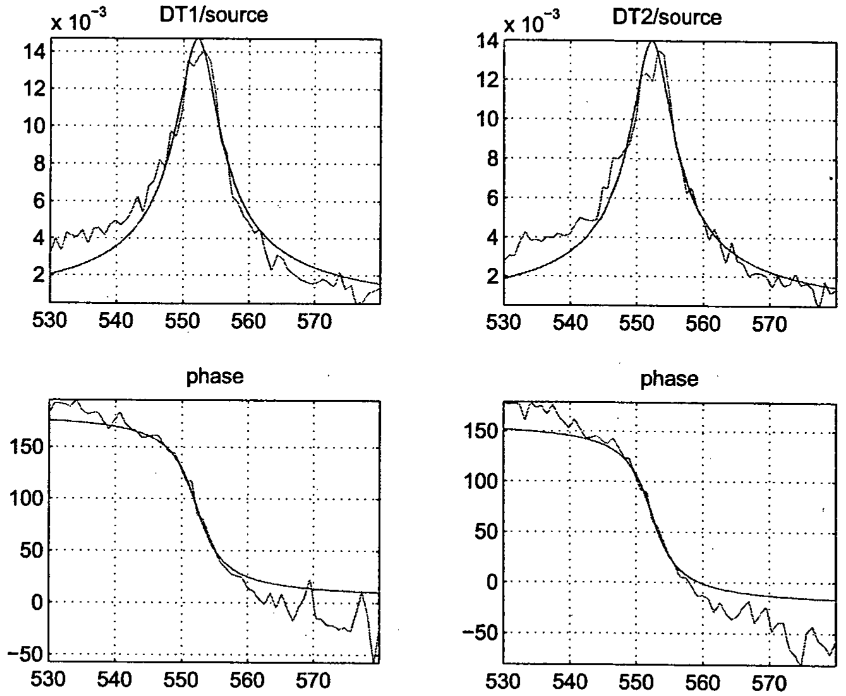

Figure 2.17: Bode plots for flutter mode $n = 2$. Experimental data and 2-nd order fits.

controller worked well. This was expected, as the phase of the frequency response of the 0-th flutter mode did not change much as one closed the throttle.

At the same operating condition (close to the 0-th flutter mode stability boundary) we conducted a control off/on/off experiment. Figure 2.24 shows 10-second time traces of one of the actuators, a strain gauge on a blade, and $DT1$ signal. One can see a significant decrease in the blade stress and blade tip movement due to 0-th flutter mode when the feedback loop is closed. Figure 2.25 shows the spectral content of these time traces when control was off and on, respectively. Note the disappearance of a sharp peak at 273 Hz at both the strain gauge and the blade arrival time difference signal spectra when control is on.

2.5.7 Experimental results: comments on model mismatch effect

The amount of damping augmentation achieved for the flutter modes with nodal diameters 0, 1, and 2, was significant. A prediction based on the 2-nd order models was that even more damping could have been achieved simply by increasing the controller gain. However, in experiment we noticed that there was an upper bound on the damping augmentation. As we were increasing the gain, the plant frequency response for all flutter modes consistently showed a magnitude plot with two resonant peaks, characteristic to a 4-th order system. Indeed, the 4-th order transfer function fits (with 4 poles and 3 zeros) to the experimental transfer functions were excellent over 40 – 50 Hz frequency band around the resonant peak for both open-loop and closed-loop plants for all values of the controller gains that we tried. For each open-loop flutter mode the four-pole pattern was similar. There were two complex conjugate pairs of poles with a similar frequency. One pair was located near the imaginary axis, more or less at the location of the poles of the second order fit. The other pair of poles was located further away. Our interpretation was that the less damped pair of poles represented the flutter dynamics,

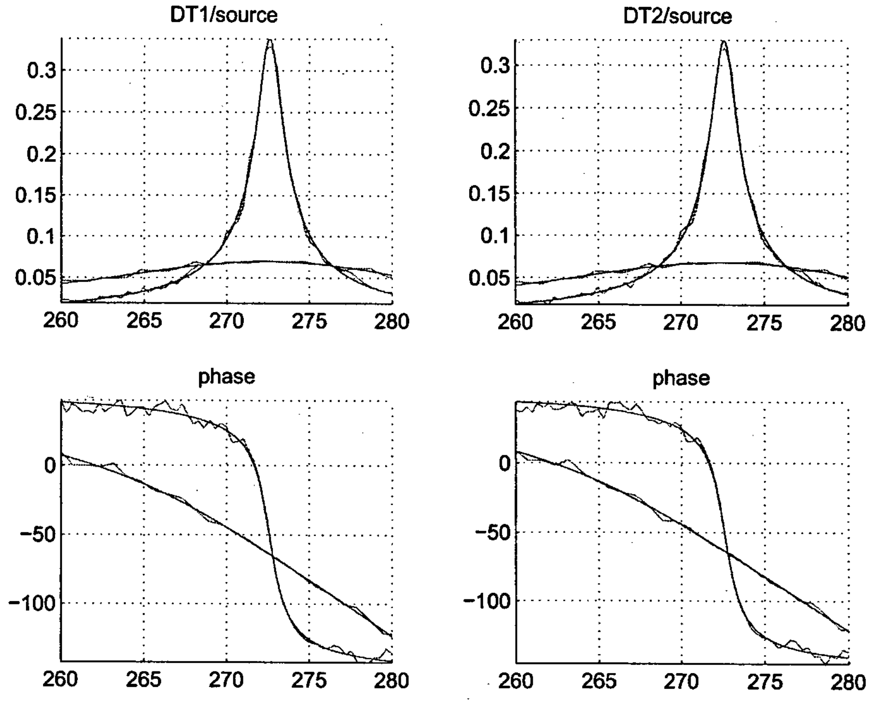

Figure 2.18: Open-loop and closed-loop Bode plots for flutter mode $n = 0$. Experimental data and 4-th order fits. δ_0: open-loop 0.018, closed-loop 0.21.

while the more damped extra pair of poles, together with an acompanying pair of zeros, accounted for the actuator dynamics and all sources of delay in the loop. It is important to note that we do not associate any direct physical meaning with the "actuator" poles and zeros. Rather than that, we interpret them as a narrow band bulk model of the phase mismatch between the experimental transfer functions and the 2-nd order fits, with the actuator phase rolloff being the major factor in that roloff.

As we increased the controller gain the poles moved towards each other, the flutter mode gaining stability and the actuator pole loosing stability. As a measure of the damping of the system we used the damping of the least damped pole in the 4-th order transfer function fit to the experimental transfer function. The optimal damping was achieved as the two pairs of poles nearly met. As we kept increasing the gain from this optimal value, the poles started to move away from one another, and one of the modes kept loosing stability.

Figure ?? show the experimetally obtained open-loop and closed-loop Bode plots for 1-st flutter mode and the corresponding 4-th order fits for 6 values of the controller gain k (with $k = 0$ corresponding to open-loop plant). The implemeted modal control was of the form

$$v_1(t) := \begin{bmatrix} \tilde{u}_{1R}(t) \\ \tilde{u}_{1I}(t) \end{bmatrix} = kK_1 \begin{bmatrix} \hat{x}_{1R}(t) \\ \hat{x}_{1I}(t) \end{bmatrix} \tag{2.77}$$

where $\hat{x}_{1R}$ and $\hat{x}_{1I}$ were the observer states corresponding to the 1-st flutter mode, K_1 was a fixed feedback matrix. The optimal value for the gain k that acheieved largest damping augmentation was around $k = 0.003$. For the value of gain higher than the optimal gain the familiar peak-splitting occured. This points out to non-minimum phase effects (actuation and flow delays).

It was important to verify that the 4-th order model would explain the root-locus behavior seen in the experiment. We simulated the controller based on 2-nd order model applied to the 4-th order

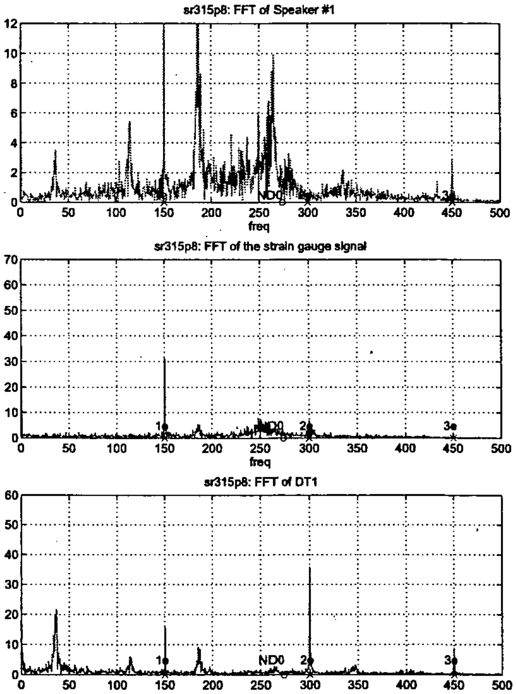

Figure 2.19: Control of 0-th nodal diameter flutter. FFT of time traces of one actuator, strain gauge, and $DT1$ signal

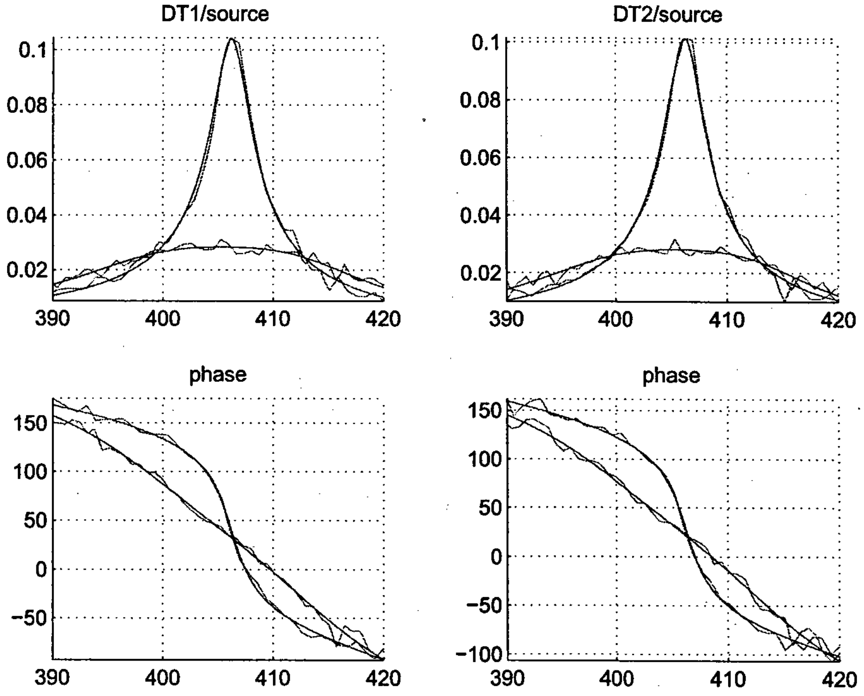

Figure 2.20: Open-loop and closed-loop Bode plots for flutter mode $n = 1$. Experimental data and 4-th order fits. δ_1: open-loop 0.028, closed-loop 0.153.

model of the 1-st flutter mode (the one that showed the biggest phase mismatch between the 2-nd and 4-th order transfer function fits to the experimental one). We plotted the corresponding root locus as well as the 6 flutter-actuator pairs of eigenvalues obtained from the 4-th order transfer function fits. One can see a qualitative agreement between the two root-loci.

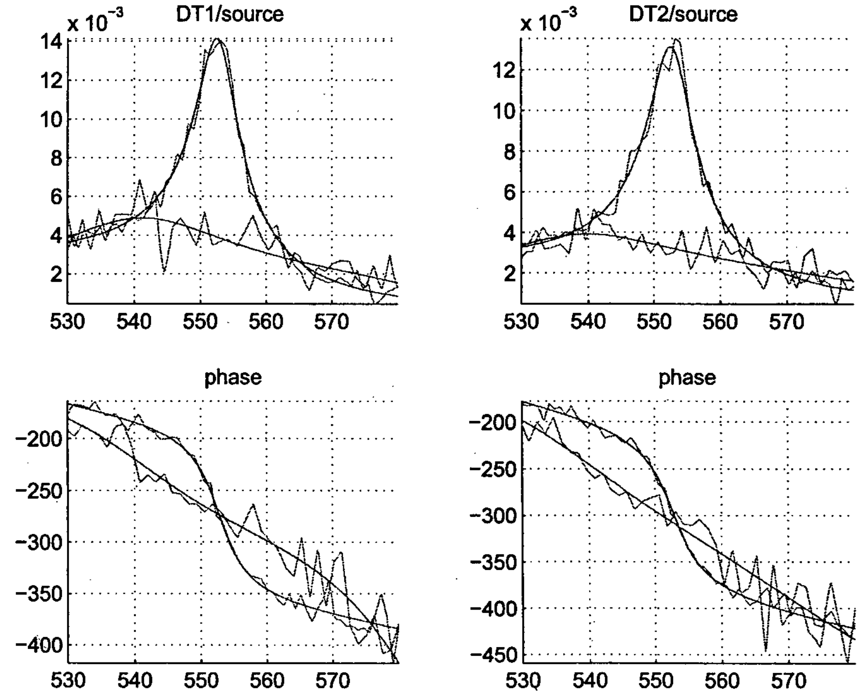

Figure 2.21: Open-loop and closed-loop Bode plots for flutter, $n = 2$, two eddy current sensors. Experimental data and 4-th order fits. δ: open-loop 0.037, closed-loop 0.174.

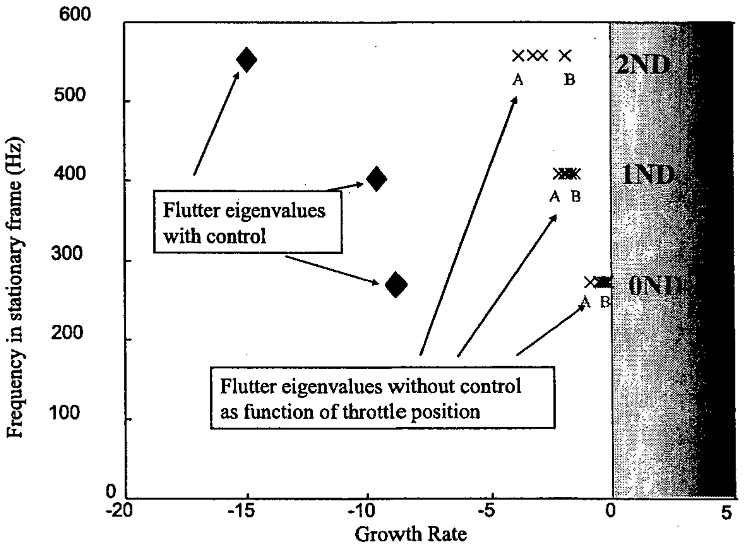

Figure 2.22: Flutter damping augmentation achieved in experiments

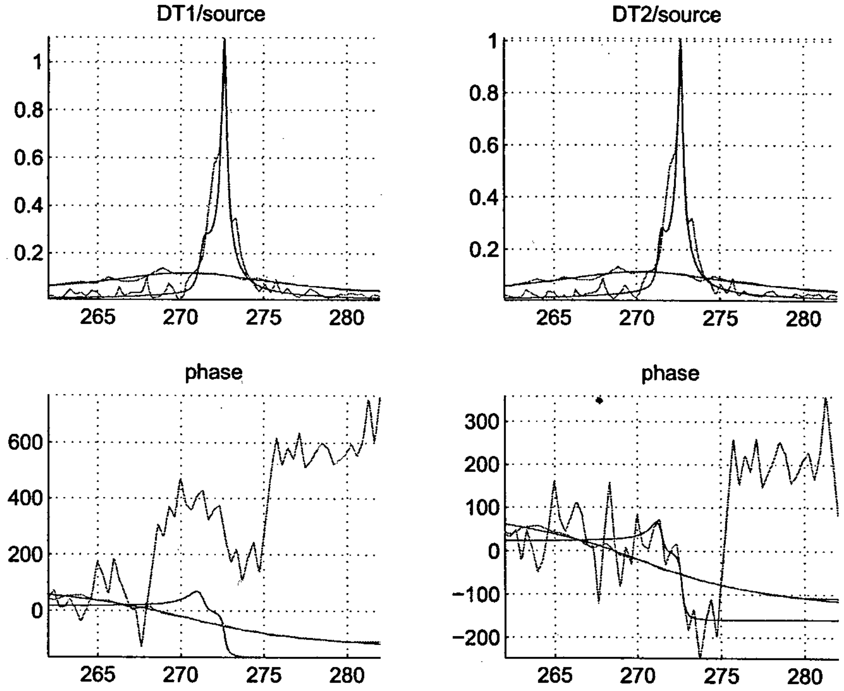
DT1/source

DT2/source

phase

phase

Figure 2.23: Open-loop and closed-loop Bode plots for flutter mode $n = 0$ close to stability boundary. Experimental data and 4-th order fits. δ: open-loop 0.007, closed-loop 0.114.

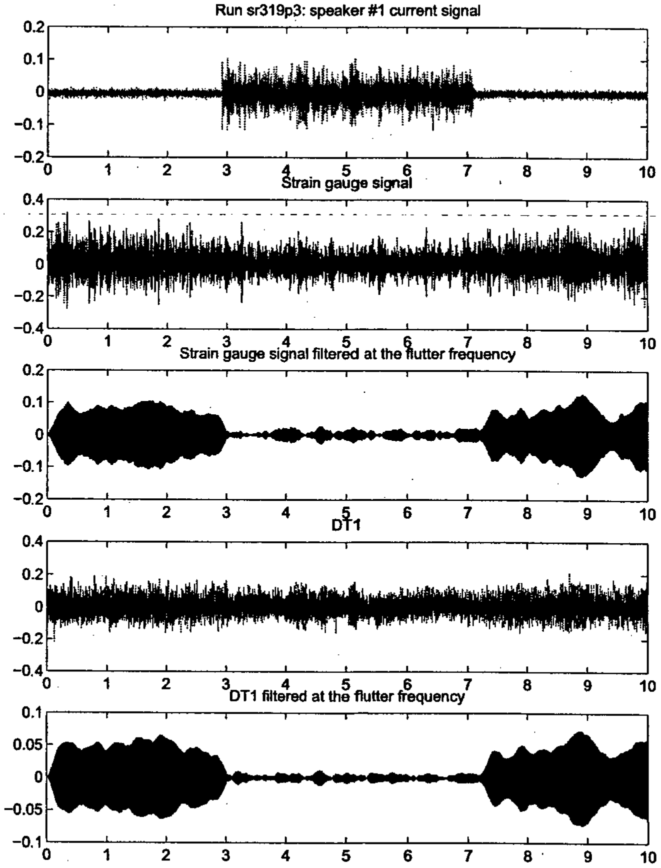

Figure 2.24: Control off/on/off experiment, 0-th nodal diameter flutter. Time traces of one actuator, strain gauge, and $DT1$ signal.

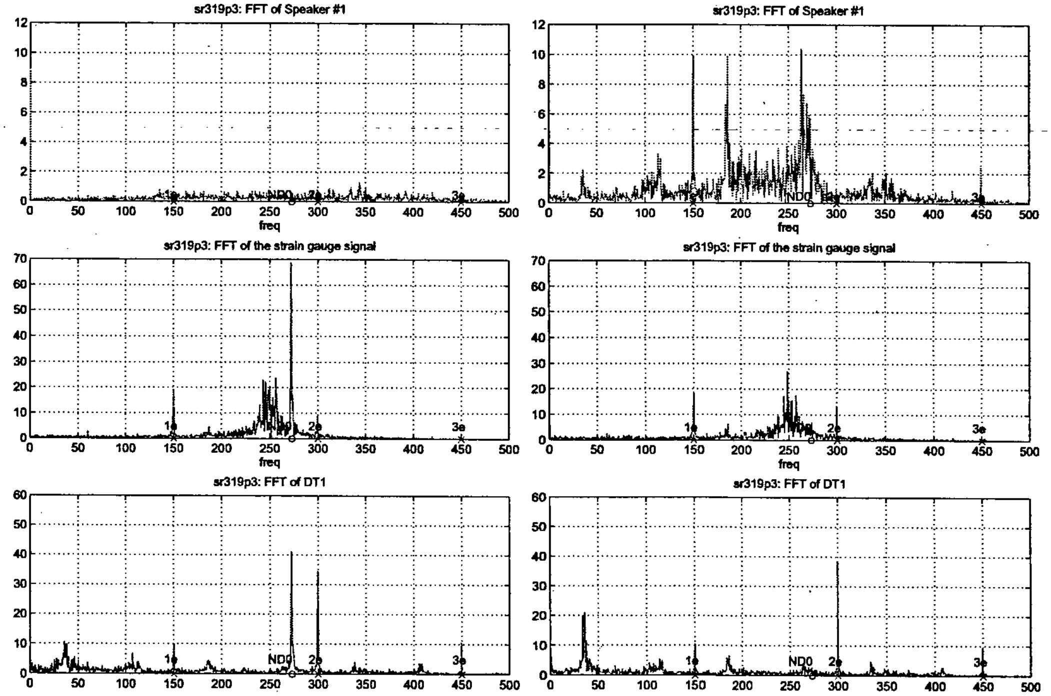

Figure 2.25: Control off/on/off experiment, 0-th nodal diameter flutter close to flutter boundary. FFT of time traces of one actuator, strain gauge, and $DT1$ signal for control off (left) and control on (right).

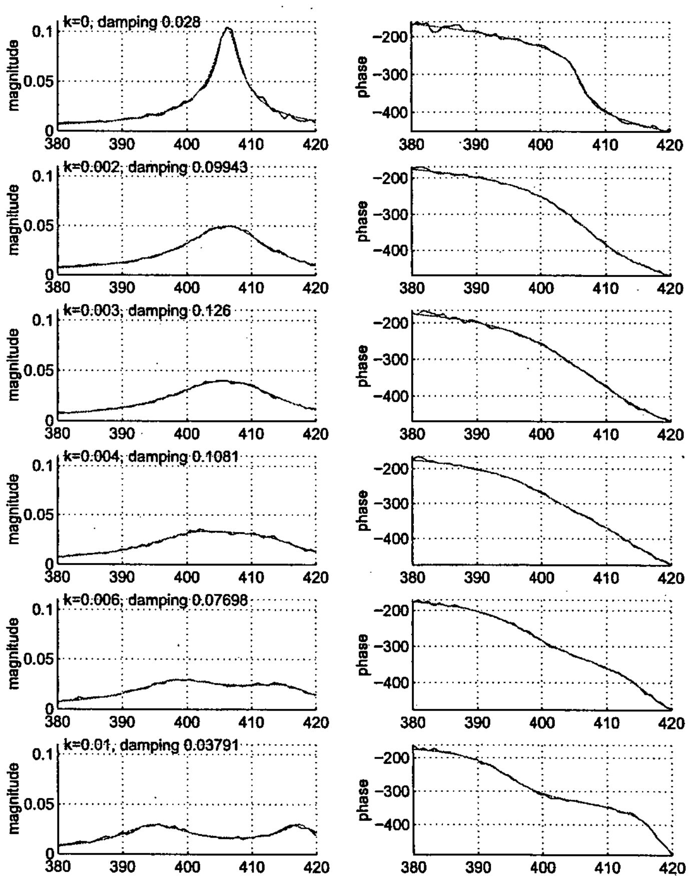

Figure 2.26: Open-loop and closed-loop Bode plots for 1-st flutter mode. Experimental data and 4-th order fits for 6 values of the controller gain. Peak-splitting appears for high gains.

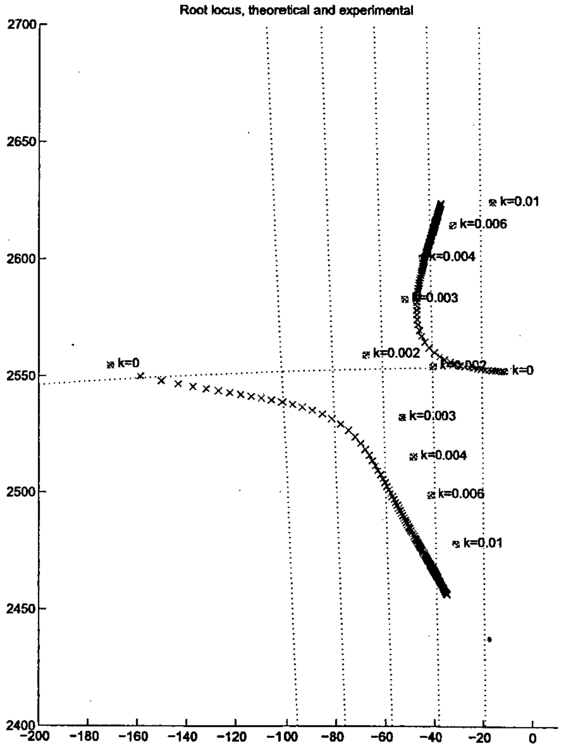

Figure 2.27: Experimental and theoretical root-locus for 4-th order plant model and controller based on 2-order order model. Experimental closed-loop poles for 6 values of the gain shown by circles and crosses. Theoretical closed-loop poles for shown by crosses.

Chapter 3

Personnel Supported

UTRC personnel: Andrzej Banaszuk, Razvan Florea, Gregory Hagen, Prashant Mehta, Marios Soteriou, Satish Narayanan, Jesper Oppelstrup, Subarrao Varigonda.

Chapter 4

Publications

4.1 Journal papers

[j1] G. Tadmor, A. Banaszuk, "Observer-based control of vortex motion in a recirculation zone", Transactions of Contol Systems Technology, 10, 2002, 749-755.

[j2] J. Cohen and A. Banaszuk, "Factors Affecting the Control of Unstable Combustors", Journal of Propulsion and Power, 19, 2003, 811-821.

[j3] Y. Wang, G. Haller, A. Banaszuk, and G. Tadmor, "Closed-loop Lagrangian separation control in a bluff body shear flow model", Physics of Fluids, 15, 2003, 2251-2266.

[j4] M. Krstic and A. Banaszuk, "Multivariable Adaptive Control of Instabilities Arising in Jet Engines," submitted to Control Engineering Practice, 2003.

[j5] S. Narayanan, P. Barooah, and J. Cohen, "The dynamics and control of an isolated jet in cross flow", AIAA Journal, 41, 2003, 2316-2330.

[j6] P. Mehta, M. Soteriou, and A. Banaszuk, "Thermoacoustic modeling of premixed bluffbody combustors: Role of exothermicity and distributed acoustics," submitted to The Combustion Institute, 2004.

[j7] B. Noack, I. Mezic, G. Tadmor, and A. Banaszuk, "Optimal Mixing in Recirculation Zones," Physics of Fluids, 16, 2004, 867-888.

[j8] I. Mezic and A. Banaszuk, "Comparison of Systems with Complex Behavior: Spectral Properties of the Koopman Operator," in print in Physica D, 2004.

[j9] A. Banaszuk, K.B. Ariyur, M. Krstic, and C.A. Jacobson, "An Adaptive Algorithm for Control of Combustion Instability, " in print in Automatica, November 2004.

[j10] T. Lieuwen and A. Banaszuk, "Background Noise Effects on Combustor Stability", to appear in Journal of Propulsion and Power, 2004.

[j11] P. Mehta and M. Soteriou, "Reduced order modeling of premixed flame dynamics in bluffbody combustors," submitted to Combustion & Flame, December 2003.

4.2 Conference papers

[c1] "Dynamics and control of a jet in cross-flow: direct numerical simulations and experiments", Peter Blossey, S. Narayanan, and T. Bewley, in Proceedings of IUTAM Symposium on Turbulent Mixing and Combustion, June 3-6, 2001, Kingston, Canada, ed. A. Pollard & S. Candel, Dordrecht, the Netherlands: Kluwer Academic Publishers, pp. 45-56.

[c2] "Experimental study of the coherent structure dynamics and control of an isolated jet in cross flow", S. Narayanan, P. Barooah, and J.M. Cohen, submitted to AIAA meeting, Reno, January 2002.

[c3-c5] A. Banaszuk, G. Rey, and D. Gysling, "Active Control of Flutter in Turbomachinery Using Off Blade Actuators and Sensors": "Part I: Modeling for Control", 2002 IFAC World Congress, Barcelona, Spain. "Part II: Control Algorithm", 2002 IEEE CDC, Las Vegas, "Part III: Experimental Demonstration", 2003 AIAA Conference, Reno.

[c6] T. Lieuwen and A. Banaszuk, "Background Noise Effects on Combustor Stability", Paper GT-2002-30062, ASME Turbo Expo 2002, June 2002, Amsterdam, The Netherlands.

[c7] P. Mehta, A. Banaszuk, and C. Jacobson, "Framework for Studying Limitations of Achievable Performance in Control of Nonlinear Combustion Processes", 2002 IFAC World Congress, Barcelona, Spain.

[c8] P. Mehta and M. Soteriou. "Combustion heat release effects on the dynamics of bluffbody stabilized premixed reacting flows", AIAA Conference, Reno 2003, 2003.

[c9] S. Narayanan and A. Banaszuk, "Experimental Study of a Novel Active Separation Control Approach", paper AIAA-2003-0060, January 2003, Reno NV.

[c10] A. Banaszuk, S. Narayanan, Y. Zhang, "Adaptive Control of Flow Separation in a Planar Diffuser", paper AIAA-2003-0617, January 2003, Reno NV.

[c11] O. Tuncer, S. Acharya, A. Banaszuk, and J. Cohen, "Side- Air-Jet Modulation for Control of Heat Release and Pattern Factor", paper GT-2003-38853, ASME Turbo Expo 2003, June 2003, Atlanta, GA.

[c12] M. Krstic and A. Banaszuk, "Multivariable Adaptive Control of Instabilities Arising in Jet Engines," 2003 ACC, June 2003, Denver, CO.

[c13] A. Banaszuk, G. Hagen, P. Mehta, and J. Oppelstrup, "A Linear Model for Control of Combustion Instabilities on Annular Domain", 2003 CDC, December 2003, Maui, HI.

[c14] P. Mehta, A. Banaszuk, M. Soteriou, and I. Mezic, Fuel control of a ducted bluffbody flame, Vol. 3: pp. 2340-2345, 2003 CDC, December 2003, Maui, HI.

[c15] P. Mehta, A. Banaszuk, and M. C. Soteriou, "Distributed control-oriented modeling of thermoacoustic dynamics in a duct," American Control Conference (ACC), June 2004.

[c16] P. Mehta, A. Banaszuk, and M. C. Soteriou, "Impact of Convection and Diffusion Processes in Fundamental Limitations of Combustion Control, " 2nd AIAA Flow Control Conference, June

2004, Portland, OR.

[c17] A. Banaszuk and Mehta, P., "Spectral Balance: Frequency Domain Framework for Analysis of Nonlinear Dynamical Systems with Noise", Accepted for 43rd IEEE Conference on Decision and Control, December 2004, Bahamas.

[c18] G. Hagen and A. Banaszuk, "Symmetry-Breaking and Uncertainty Propagation in Reduced Order Thermo-acoustic Model", Accepted for 43rd IEEE Conference on Decision and Control, December 2004, Bahamas.

[c19] S. Varigonda, "An Iterative Method for Propagation of Probability Distributions in Feedback Systems", Accepted for 43rd IEEE Conference on Decision and Control, December 2004, Bahamas.

[c20] K. Teerlinck, G. Hagen, A. Banaszuk, J. Lovett, J. Cohen, A. Ateshkadi, B. Kiel, "Experimental Demonstration of Control of a Thermoacoustic Instability in a Three-Flameholder Rig," submitted to AIAA conference, January 2005, Reno NV.

4.3 Reports

P. Mehta, G. Hagen, A. Banaszuk, M. Soteriou, B. Noack, and G. Tadmor, "A Galerkin model for reacting bluffbody flow", UTRC internal report, 2003.

4.4 Invited Sessions

The following invited sessions were organized with AFOSR support and contain AFOSR-funded papers:

2003 CDC, Maui: Flow and combustion control. Organizers: G. Tadmor and A. Banaszuk.

2004 CDC, Bahamas: Uncertainty Propagation: Applications. Organizers: M. Huzmezan and T. Runolfsson.

2004 CDC, Bahamas: Uncertainty Propagation: Theory and Tools, Organizers: T. Kalmar-Nagy and I. Mezic.

4.5 Talks

P. G. Mehta and M. Soteriou, Reduced Order Modeling of Premixed Flame Dynamics in Bluffbody Combustors, 56th Annual Meeting of the American Physical Society: Division of Fluid Dynamics, November 2003, NJ.

M. C. Soteriou and P. G. Mehta, Lagrangian model for bluffbody-stabilized premixed combustion for flow control, 55th Annual Meeting of the American Physical Society: Division of Fluid Dynamics, November 2002, Dallas TX.

P. G. Mehta, M. C. Soteriou, and A. Banaszuk, Model-based investigation of control of thermoacoustic instability using flow control, 54th Annual Meeting of the American Physical Society: Division of Fluid Dynamics, November 2001, San Diego CA.

Chapter 5

References

From: Dr. Andrzej Banaszuk
Principal Research Engineer
United Technologies Research Center
411 Silver Lane, MS 129-15
East Hartford, CT 06108
(860) 610-7381 FAX: (860) 6610-1016
banasza@utrc.utc.com

To: Lt Col Sharon Heise, USAF, PhD
Program Manager, Dynamics & Control
AFOSR/NM
4015 Wilson Blvd, Rm 713
Arlington, VA 22203

Dear Dr. Heise:

Enclosed is a final report for AFOSR contract F49620-01-C-0021 "Control of Mixing in Shear Flows". Please let me know if the report is acceptable in its current form. Upon receipt of the your acceptance letter copies of the report will be sent to ACO and DTIC.

Sincerely yours,

Andrzej Banaszuk
Principal Research Engineer
United Technologies Research Center